DEVELOPMENT OF AN EXPOSURE TOOL FOR LITHOGRAPHY ON TILTED AND CURVED SURFACES USING A SPATIAL LIGHT MODULATOR

THESIS

Presented to the Graduate Council of
Texas State University-San Marcos
in Partial Fulfillment
of the Requirements

for the Degree

Master of SCIENCE

by

Javad Rezanezhad Gatabi

San Marcos, Texas
December 2013

DEVELOPMENT OF AN EXPOSURE TOOL FOR LITHOGRAPHY ON TILTED AND CURVED SURFACES USING A SPATIAL LIGHT MODULATOR

Committee Members Approved:

_____
Wilhelmus J. Geerts, Chair

_____
Ravi Droopad

_____
Nikoleta Theodoropoulou

_____
Dan E. Tamir

Approved:

_____
Andrea Golato
Dean of the Graduate College

FAIR USE AND AUTHOR'S PERMISSION STATEMENT

Fair Use

Duplication Permission

For mom and dad

& my late uncle Reza

ACKNOWLEDGEMENTS

The work reported on in this thesis was supported by a grant from (NSF 0923506). In addition I would like to thank the department of Physics, the College of Science, and the Texas Section of the American Physical Society for financial support to attend two TSAPS meetings and the march 2013 APS meetting in Baltimore. Many people and organizations have contributed to this thesis. First of all Applied Micro Devices need to be thanked for donating the laser beam writer. Dr Anup Bandyopadhyaya for plating a convex and concave lens with titanium and provide me with two model curved surfaces. Shane Arabie (Engineering Technology) for milling work on various parts, for helping me fix the mechanical part of the z-stage of the opttical microscope, and for his advice, interest and help on various aspects of the project. Dr. Stefan Osten and Andreas Hermerschidt (Holoeye Inc.) for their help and advice when implementing the traditional Gerchberg-Saxton algorithm. Altaf Ramji (PCO-Tech) for his help with the PCO.edge camera, i.e. drivers and memory issues. Lisa Safran (Kopin) for special order to provide us with an LCD without color filters. Prof. Dr. Vishu Visnawathan (Electrical Engineering) and Dr. Pedra Gelabert (Texas Instrument) for donating two Lightcrafters to the project and for their encouraging remarks.

A special thank to my advisor Dr. Ir. Wilhelmus J. Geerts, who provided me with valuable research opportunities on his research lab and for his encouragement during the

past two years. I would like to thank my committee members, Dr. Ravi Droopad, Dr. Nikoleta Theodoropoulou, and Dr. Dan E. Tamir for their wonderful advice.

This manuscript was submitted on August 9, 2013.

TABLE OF CONTENTS

Page

LIST OF TABLES

Table **Page**

LIST OF FIGURES

Figure **Page**

ABSTRACT

DEVELOPMENT OF AN EXPOSURE TOOL FOR LITHOGRAPHY ON TILTED AND CURVED SURFACES USING A SPATIAL LIGHT MODULATOR

by

Javad Rezanezhad Gatabi

Texas State University-San Marcos

December 2013

SUPERVISING PROFESSOR: Ir. Wilhelmus J. Geerts

This thesis is on research to develop a new laser lithography exposure tool for use on non-flat substrates. Such a tool does currently not exists as commercial equipment used in the electronic industry uses high numerical aperture (NA) lenses to create patterns with critical dimensions down to 22 nm on very flat substrates (+/- 100 nm). The ability to pattern thin films on top of curved substrates with large topography differences allows for the development of new products and devices: it enable the integration of high density integrated electronics on non planar samples such as those created by integrated optical, micromechanical, and micromagnetic technologies, resulting in the realization of smart sensors and actuators. The tool also opens up new opportunities in materials characterization: the ability to place electric contacts on a 20 micron single crystalline

grain of a polycrystalline sample allow us to separate bulk and grain boundary contributions to the electric transport properties of polycrystalline materials. An existing Florod laser beam writer used for lithography on flat substrates was modified on three different points to allow for the exposure of non-flat substrates: (1) The optical throughput of the system wass optimized to allow for real-time determination of the photoresist film thickness from the reflection spectrum of the sample; (2) A high resolution optical light pattern generator was installed on the system and allows for the determination of the sample's topography by measuring the point spread functions and the modulation transfer functions from the sample-microscopy system. The installed light pattern generator is based on a Kopin high resolution amplitude spatial light modulator (1.5 micron resolution on the sample) and a LED light source; (3) A Holoeye phase only spatial light modulator (SLM) was installed on the system to allow for imaging on tilted and curved substrates. Three different beam shaping methods were investigated: (1) implementation of a single lens or multi-lens array on the SLM to allow for electronic focus control across a curved or tilted sample. The controllable focus range is up to 16 mm for the Pluto modulator and up to 0.7 mm for the LC2002 modulator. For large single SLM lenses the system is limited by aberrations caused by quantization, pixellation, and curvature of the modulator. Implementation of an SLM multilens array whose lenses have different focal distances increases the depth of field at the expense of a larger diffraction limited spot size; (2) implementation of a tilted lens function in the SLM allows for imaging on tilted samples. Preliminary experiments however show that the imaging quality is limited when using the SLM lens in combination with a real object; (3) implementation of the Gerchberg-Saxton algorithm to calculate the SLM optical field

required to generate a certain intensity pattern on a tilted sample. The classical Gerchberg Saxton algorithm that was developed for Fraunhofer diffraction was adapted for finite projection distances and tilted samples. The algorithm appears to be stable and converging for the tested patterns and shows a light focussing improvement with respect to the classical algorithm.

CHAPTER I: INTRODUCTION

This chapter provides a short introduction to lithography as used in the semiconductor industry. The motivation for research and devlopement of a lithography exposure tool that will enable nanostructuring of non flat samples is followed by a summary of the work of others on this topic. In the second part of the chapter the modifications required to a standard lithography exposure tool to make it suitable for lithography on 3D substrates are described. The chapter finishes with how these modifications were addressed in this thesis work.

Lithography

Lithography is an important step for the fabrication of electronic components. In the lithography process, the blue-print of the circuit diagram is transferred onto the wafer by nanopatterning conducting, semiconducting, and insulating thin films on top of the wafer. Currently the photolithographic process steps can contribute up to 50% of the wafer costs. In 2013 the most advanced lithography equipments were able to expose up to 250 wafers per hour and write 2.6E12 pixels per field exposure (26x33 mm^2). Note that the number of pixels of a lithographic exposure tool is more than 6 orders of magnitude larger than that of a professional DSLR camera lens. The following figure shows the typical critical dimensions and the number of pixels written by a commercial

ASML exposure tool over the last three decades (ASM Lithography founded in 1984 as a joint venture between Advanced Semiconductor Materials International and Philips became independent in 1987 and adopted the name ASML).

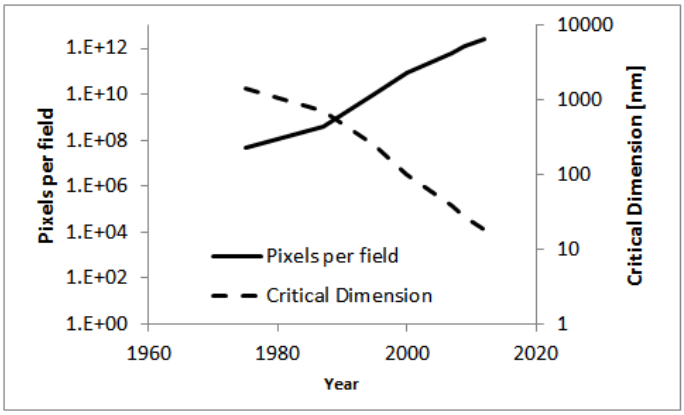

Figure 1.1: Critical dimensions and the amount of pixels written by exposure tools developed by ASML over the last three decades

John H. Bruning, Optical Lithography … 40 years and holding, Proc. of SPIE Vol. 6520, 652004, (2007).

The push to achieve smaller features is mainly driven by reducing the cost per transistor and increasing the speed of integrated circuits. Since 1990 the cost per transistor has decreased by approximately 30% per year and the cost per pixel of the lithography has decreased by approximately 35% per year. The size reduction has other advantages like lower power consumption. This size reduction was accomplished by decreasing the wavelength of the exposure light, increasing the numerical aperture of the objective lenses of the exposure tools, and improving the properties of the photoresist. A significant improvement was also accomplished by implementing planarization steps between various process steps, allowing for large numerical aperture lenses to be introduced in the exposure equipment. In 2013, the electronic industry can mass produce ICs with a critical line width below 22 nm on very flat substrates (the depth of field of

the 22 nm node is around 200 nm). Memories with 22 nm features were first commercially produced in 2008 and since 2012, microprocessors are also made with features that small. The research community is currently working on finding solutions to create electronics with 14 nm critical dimensions. Various methods such as extreme UV (EUV) and Electron Beam lithography are investigated to mass fabricate ICs with features below 22 nm.

The basic process flow of lithography is outlined in Figure 1.2. There are 7 main steps that define the photo-lithography process.

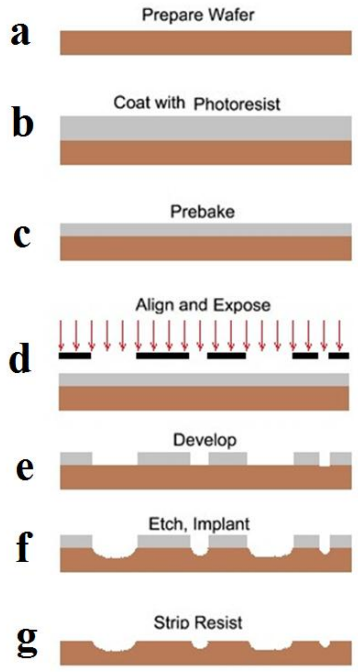

Figure 1.2: 7 main steps for lithography process

In the first step, the surface is heated up to remove the moisture and it is cleaned with certain chemicals (Fig. 1.2.a). In the second step, the surface of the wafer is coated with the photo-resist using the spin coating technique. In this technique, a certain amount

of photo-resist material is dispenced on the surface and the wafer is spun with a high rotational velocity. In this way, a uniform thin layer of photoresist covers the surface (Fig. 1.2.b). Important parameters of the spinning process that define the photoresist thickness are angular acceleration, final spin speed and the total duration of the spin process. The thickness of the photoresist layer also depends on the viscosity of the photoresist as well as the exhaust connected to the spinner. The angular acceleration mainly influences the homogeneity of the layer across the wafer surface. In case of non-rotation-symmetric substrates, the resist forms a pronounced edge bead near the substrate edges due to the strong air turbulences. After spinning, the wafer is prebaked to remove the photoresist solvent and make the sample less sticky (Fig. 1.2.c). It is important to keep the parameters of the spining and pre-bake constant as both have a strong influence on the photoresist film thickness. A reproducable thermal contact between the wafer and the hot plate during the pre-bake by means of a vacuum chuck is essential to create a consistent photoresist film thickness across a sample series. In the fourth step, the mask containing the blue print of the microstructuring is aligned, followed by the exposure.(Fig. 1.2.d). Exposing the photoresist material by a light beam causes a chemical change in the photoresit material; for positive (negative) photoresists, the exposed (unexposed) regions are soluble in the developer, creating windows in the photoresist layer. (Fig. 1.2.e). The exposed surface of the wafer is then etched by chemicals (wet etch) or by a plasma (dry etch) (Fig. 1.2.f) creating the desired microstructure on the wafer. The remaining photoresist material is then removed using wet chemicals or using a plasma containing oxygen (Fig. 1.2.g).

The mask to create the desired pattern determines the the resolution and quality of the product and it is a costly part of the lithography process. In mass production, it is reasonable to use expensive masks. However, in prototyping, it is not reasonable to spend lots of money to fabricate a mask which is used only for making several samples. Hence, using a focussed laser beam writer and directly writing the pattern onto the photoresist is an economical alternative used for rapid prototyping or when producing ICs with small production volumes. Recently, researchers have accomplished optical beam lithography creating 9 nm features [1] which is approaching the capabilities of electron beam lithography, an expensive alternative. The disadvantage of maskless lithography is the slow throughput related to the serial character of the writing process: The pattern is written one pixel at a time. To ameliorate this issue, researchers have recently started to incorporate digital mirror arrays [2] and phase plates [3] into the exposure equipment, writing millions of pixels simultaneously. Although those fast maskless lithography exposure tools are very popular for the mass production of printed circuit boards, they still seem to lack the high resolution of conventional exposure tools which use masks.

Note that since the seventies above mentioned direct write approaches are also used for making the masks.

Lithography on Non-flat Substrates.

All commercial exposure tools are meant to be used on flat substrates. In fact part of the resolution improvements of lithography exposure tools have been realized by the introduction of higher NA lenses and more homogeneous illumination devices (NA of 22

nm node is 1.35). These improvements require flatter samples. Lithography exposure equipment that can provide us with a mean to create nano-structures on non-flat samples would result in new research and development opportunities and possibly new products. Such tool could for example be used to integrate electronics on devices created with non-flat technologies such as multi-lens arrays, electro-optical devices, magnetic sensors and actuators, or micro-mechanical devices. Integration of all those non flat technologies with electronics allows for the development of new novel smart and fast devices. It is expected that a lithography exposure tool for non-flat substrates would also create new measurement strategies in materials research. For example such tool would allow us to put contacts on a 20 um single crystalline grain for electrical characterization resulting in a measurement method to separate the contributions of defect and grain boundary scattering to the resistivity of poly crystalline materials.

Current research and applications of lithography on non-flat substrates are scarce. Ball Semiconductor has developed special equipment for lithography on 1 mm diameter silicon spheres for novel electronic devices, including microwave and solar cell applications. Since the total surface area of a sphere is about 3 times larger than the area of a flat substrate this approach can reduce the associated cost. Other advantages of their technology are the capability to realize high inductors on the spheres, and the option to create 3D devices such as 3D CCD camera and 3D accelerometers. Their lithography system uses six digital micro mirror devices (DMD) each of which consists of an array of 800x600 micro-mirrors and functions as an electronic mask. Each DMD is projected by a micro lens system on a part of the sphere. Six of these devices approximately cover the complete sphere. Although ingenious, their setup can only work for spheres with a

diameter of around 1 mm [4]. Several researchers used projection lithography to create structures on cylindrical surfaces [5, 6], and on curved surfaces of revolution used for MEMS or integrated optics applications [7]. Other technologies, such as nanoimprint, have been used on concave or convex lens surfaces [8, 9], and on cylindrical surface [10, 11]. Direct electron beam lithography has been applied to create aspheric lenses on concave mirror surfaces [12]. To keep the electron beam focused on all positions on the substrate and to keep the electron dose constant, the electron beam was placed at a working distance that is equal to the radius of curvature of the sample. An extensive literature search found only a handful of research groups that are using a laser beam writer for lithography on simple non-flat substrates [13, 14, 15]. Radtke et al. use a modified DWL400 laser beam writer [15]. They extended the instrument with a tilting stage that can tilt the sample +/- 10^{o} along two orthogonal axes, allowing direct writing on concave and convex surfaces [15]. Snow et al. incorporated a rotary stage in a conventional laser beam writer setup. This enables writing on a set of aligned cylindrical glass fibers [14]. Their paper discusses the effect of substrate curvature on the delivered exposure dose. Zhang et al. use a traditional laser beam writer with XY-control of the substrate and z-control of the objective to write a grating on convex lens surfaces [13]. Before starting with the writing process, they center the laser beam in the middle of the lens. Next, in order to keep the laser beam more-or-less focused on the surface during the writing process, they use an algorithm that simultaneously scans in the X and Z directions. Their system does not make automatic corrections of the exposure dose, or the line width of the sloped parts of the substrate. Hence, they can only produce uniform gratings on simple, weakly curved, non-flat substrates. Recently, Chen et al. presented a

new mathematical model of the optical field distribution when exposing photoresist material on convex substrates [16]. Romero et al. used a laser beam writer to create a multi lens array on a curved surface [17]. In both of these works, the photoresist layer on the substrate surface with known curvature is also exposed by a laser beam.

Lithography on non-flat substrates is not trivial for several reasons. Spinning can no longer be used to apply photoresist to non-flat samples and one should use other methods such as for example an air-brush, high pressure evaporation, or a simple eye-dropper. Also the exposure tool need to be adapted since because of the non-linear chemical response of photoresist to the exposed light intensity, the laser beam intensity should be adjusted on curved surfaces or in areas that have a different photoresist film thickness. Hence, the laser lithography on tilted or curved surfaces has three main modifications with respect to a lithography tool used on a flat substrate (see Fig. 1.3). First of all the topography of the surface on any specific point within the optical field of the microscope needs to be determined to identify the local slope and curvature of the sample. In other words a real-time topography monitor needs to be installed on the exposure tool. Second the exposure tool need to determine the photoresist thickness at various points on the surface. It is very likely that the photoresist thickness is not homogeneous across a sample with large topography differences. The installation and development of a photoresist thickness monitor was the subject of a previous thesis project [20]. Third the intensity of the laser source needs to be adapted using the topography and photoresist film thickness measurement data to guarantee a constant exposure dose independent of the local surface curvature or the local photoresist film thickness; in other words the focussed laser beam writer need to be modified so it is able to focus the beam uniformly

on a tilted or curved. Although this thesis work has mainly focussed on the last problem, i.e. shaping the laser beam and wrapping the 2D blue-print around a 3D surface, two significant contributions were made in support of the first two required modifications: (1) New hardware, software and optics was developed and integrated in the system to allow for topography measurements [18,19]; (2) The optical throughput of the alignment beam was increased to improve the performance of the photoresist thickness monitor and allow for faster photoresist film thickness measurements [20]. Both modifications are described in chapter 2 while the rest of the thesis focusses on the laser beam shaping part of the project using a phase only spatial light modulator (SLM). Three different methods were explored for beam shaping: (a) the SLM was used to implement an array of multi-lenses each with their own focal distance imaging a different part of the mask (chapter IV); (b) the SLM was used to implement a titled lens which allows for imaging on a tilted surface similar to the tilt and shift lenses that are used by professional photographers (chapter V); (c) the SLM was used to implement a modified version of the Gerchberg-Saxton algorithm to allow for the calculation of the SLM's optical field for the projection on a tilted surface (chapter VI).

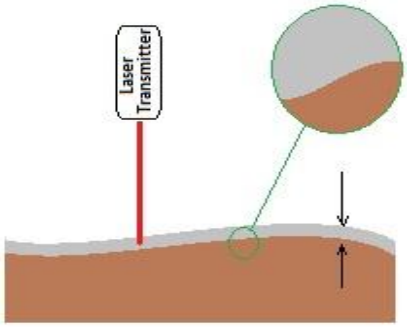

Figure 1.3: The main three parts of the laser lithography system: (a) beam shaping unit; (b) topography monitor; (c) photoresist film thickness monitor.

CHAPTER II: LASER BEAM SETUP

This chapter introduces the Florod laser beam system that was used for experiments. The Florod laser beam writer is originally designed for lithography on non-flat substrates. To prepare the system for the present study, some modifications were done on the Florod laser beam writer. These modifications consist of: upgrading the optical elements to use a shorter wavelength laser and preparing the system for faster photoresist film thickness monitoring, installing new hardware and optical components in support of the topography measurement unit, and installing the SLM setup. In this chapter, first, the system specifications are outlined and then the modifications made to the system are reported.

Florod Laser Beam Writer

In this research, a Florod Laser Beam Writer as shown in Figure 2.1, is modified for laser lithography on curved surfaces at the physics department of Texas State University. The device was manufactured by the Florod Corporation and was designed to be used with an argon laser working in the wavelength range of 454nm-514nm.

Figure 2.1: Florod Laser Beam Writer at the physics department of Texas State University

Figure 2.2 shows the optical diagram of the Florod Laser Beam Writer. The design is based on an infinity corrected optical microscope and uses Mitutoyo long distance objectives. The system consists of three different parts:

(a) The imaging column (see left Fig. 2.2.) consisting of the sample, the objective, the tube lens (lens 2), and a fast and sensitive camera (pco.edge). The tube lens has a focal distance of 120 mm resulting in a magnification of 30x for a 50x objective.

(b) The background light column consisting of a light source, a compound lens (lens 1), the objective and the sample. This path is designed for the background light which keeps the whole sample visible under the microscope.

(c) The exposure/alignment column consisting of two light sources, an aperture, the laser beam lens (lens 3), the objective, and the sample. This light path is meant to create and a focused laser beam that is used to exposure the photoresist and a focused white light beam that is used to measure the thickness of the photoresist layer. Two light beams are coupled into the system using semi-transparent

mirrors: the light of a collimated wide band halogen bulb and the light of a 405 nm laser. The wide band light source is used to measure the thickness of the photoresist layer of the sample from the reflection spectrum: the presence of interference maxima and minima is used to estimate the photoresist film thickness. More details on the thickness monitor can be found in [20]. The laser is used to expose the photoresist. The photoresist is not sensitive at the wide band optical source. The laser beam size on the sample, which is positioned on a computer controlled x-y stage, depends on the objective. It is 1.7μm-10μm using the 50X objective, 4.25 μm-25μm using the 20X objective, and 17μm-100μm using the 5X objective. The size of the laser beam is determined by a variable aperture consisting of two variable slits oriented perpendicular to each other. Currently this manual aperture is replaced by an electronic aperture based on a digital mirror device of Texas Instruments. Once completed this will allow for computer control of the size and the exact position of the exposure/alignment beam.

The area between the objective, lens 1, lens 2, and lens 3 is considered to be the infinity space. The pco-edge camera, on top of the system, can be used to take images of the alignment beam and the sample (see insert of Fig. 2.2).

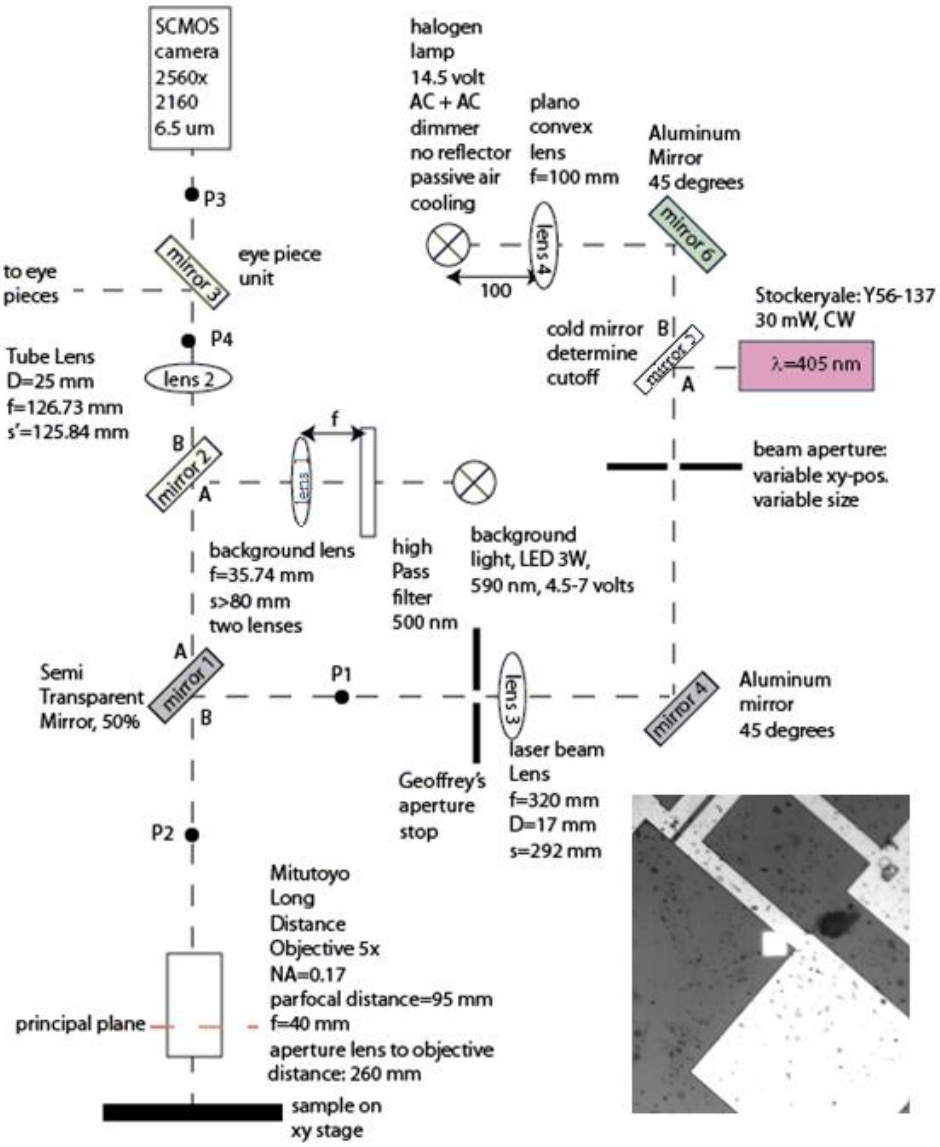

Figure 2.2: Optical diagram of the Florod Laser Beam Writer

The insert shows a picture taken with the system's camera from an electronic circuit positioned on the stage. The square in the middle of the image is the alignment beam.

Modifications for Topography Monitor

To measure the surface topography of the sample a light pattern generator was installed in the background light optical beam of the setup. This generator allows for the projection of a specific light pattern onto the sample. The optical response of the system is measured by taking images of the projected light pattern on the sample using the CCD camera installed on the system. As the optical response of the system depends on the sample slope and the out of focus error, it is possible to determine the sample topography from those measurements. Typical test patterns are arrays of delta-functions and periodic gratings. The former allows for the determination of the point spread functions while the latter allows for the determination of the modulation transfer function of the sample-microscope system. [18, 19].

To generate the pattern for topography measurements several options were considered, i.e. a permanent mask, a 3D mask consisting of a stack of microscope slides each containing a mask, and an electronic mask. To get as much flexibility as possible the latter option was implemented. An amplitude modulator LCD was placed in the background light optical beam at the focal point of lens1 (see Fig. 2.3). To reduce the heat load of the light source on the LCD the original halogen background light bulb was replaced by a 3Watt/12 volt commercial automobile LED bulb (Super Bright LEDs). Experiments were performed with three different colors, i.e. orange (1156-ALX3: 590 nm)), red (1156-RLX3: 617 nm), and white (WLX3). The AC-power supply of the light source was replaced with a DC lab supply. For the electronic mask preliminary experiments were performed with an RGB LCD that was pulled out from a working projector ($100- Shift 3 Lightblast Entertainment Projector from CVS Pharmacy). This

LCD had a pixel size of 126 x 63 um and used a standard video input. The control electronics and its power supply were also removed from the projector and incorporated in a RadioShack project box (see Fig. 2.3 a). The Radio-Shack box was mounted on a manual xy-stage and then incorporated in the system (see Fig. 2.3b). The LCD was controlled via a video-card in the back of the computer.

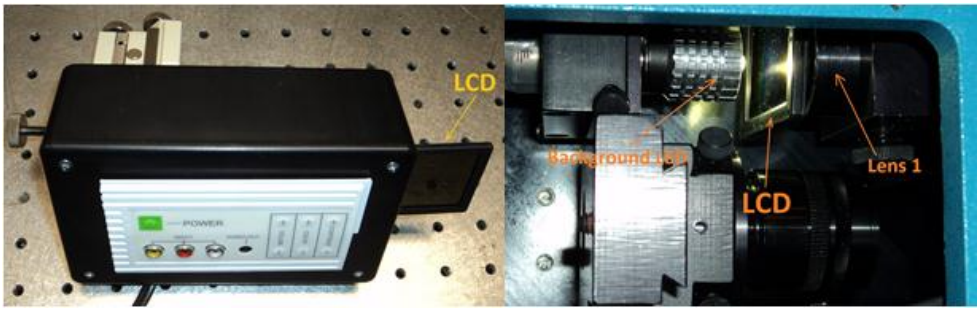

Figure 2.3: The RGB LCD unit incorporated in the RadioShack project box (left) and the LCD incorporated in the laser beam writer (right)

Figure 2.4 shows an image taken with the system camera after installing the LCD in the background light column. The effective pixels for the transferred pattern are limited to 8X12 pixels because of the spherical aberration of lens 1 (Fig. 2.2) and the large pixel size of the LCD. Figure 2.4a shows an image taken with the system camera when a flat sample is positioned on the xy-stage and a grating pattern is loaded on the LCD. In between the grating lines, the individual LCD pixels are visible. As this LCD has the red, green, and blue color filters integrated in each consecutive pixel, the pixels showed up with different grey scale values on the monochrome CCD image. Figure 2.4b shows an image taken with the system camera when a concave sample is positioned on the xy-stage and a white image is loaded on the LCD. It is clear that only the pixels in a ring are focused while the pixels at the center of the image are out of focus. It is also clear

that the resolution of a topography monitor based on this LCD is limited by the large pixel size.

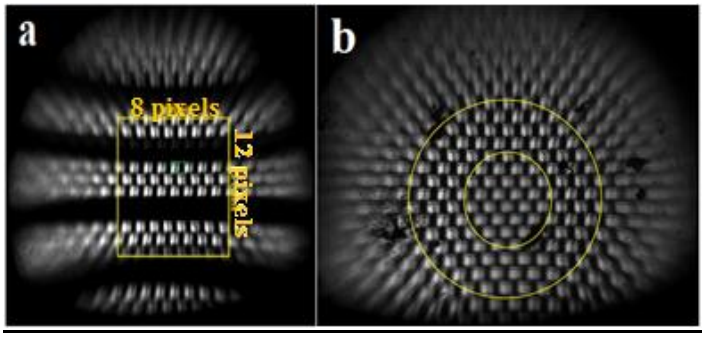

Figure 2.4: The maximum effective pixels for the transferred pattern and a sample of transferred pattern on a concave sample

Figure 2.5 shows the pixel size of the used LCD when the surface of the LCD is imaged by an optical microscope. Each pixel is considered to consist of three sub-pixels each with their own color filter. Note the control electronics in the top of each sub-pixel.

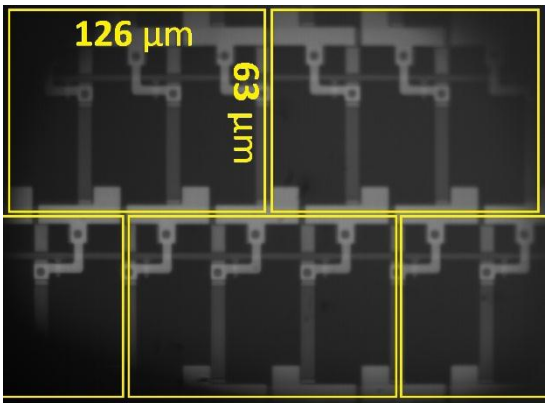

Figure 2.5: The pixel size of the first amplitude modulator LCD used for transferring the pattern onto the surface of the sample

To generate light patterns with more details, the first LCD was replaced with a "KOPIN" LCD that is normally used in the viewfinder of a video camera (KCD-VDNC-BA monochrome CyberDisplay). The pixel size of this Kopin LCD is 4.7μm x14.1μm; an order of magnitude smaller than the pixel size of our first prototype. Furthermore no color filters were incorporated in the device resulting in a monochrome pixel field of 1920x480 pixels controllable by a standard VGA interface. Although the Kopin LCD includes a low intensity backlight source clamped on it, experiments showed that its intensity was too low to allow for short camera integration times. Therefore, the original Kopin backlight was replaced with a higher power LED array (C6060 LED array). To collimate the beam, a lens (Double convex, Diameter: 25mm, Focal Length: 20mm) is placed between the light source and the LCD. Figure 2.6a shows the LCD inserted in the microscope setup. The LCD is mounted on a xyzθ stage in order to have an accurate positioning of the modulator. A Labview program is written to position and rotate a bit map image on the Kopin LCD. Figure 2.6b illustrates an image of the LCD taken by the camera on top of the microscope after loading a black cross image into the LCD. Having much smaller pixels, the images taken from the light patterns do not show the individual LCD pixels. Figure 2.6c shows a magnified area of the image shown in Figure 2.6b. It shows a fine line pattern caused by the height of the LCD pixels that is still being resolved by the optics of the laser beam writer (14.1μm which corresponds to a 1.41 um on the sample).

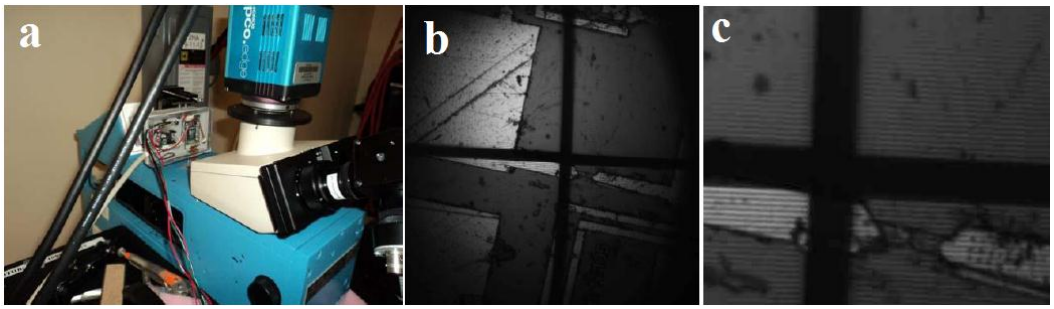

Figure 2.6: (a) The new LCD inserted in the background light path of the setup; (b) The image of LCD taken by the system camera after loading a white image with four black squares on the LCD; (c) The image of LCD taken by the system camera after loading a white image with a black cross on the LCD.

The figure below shows a series of images taken with the new light pattern generator. A convex lens plated with titanium was used as a substrate. The light pattern consisted of an array of rectangular functions each of 3x3 um large and each separated by 15 um in the x and the y-directions. Each image was taken at a different objective to sample distance.

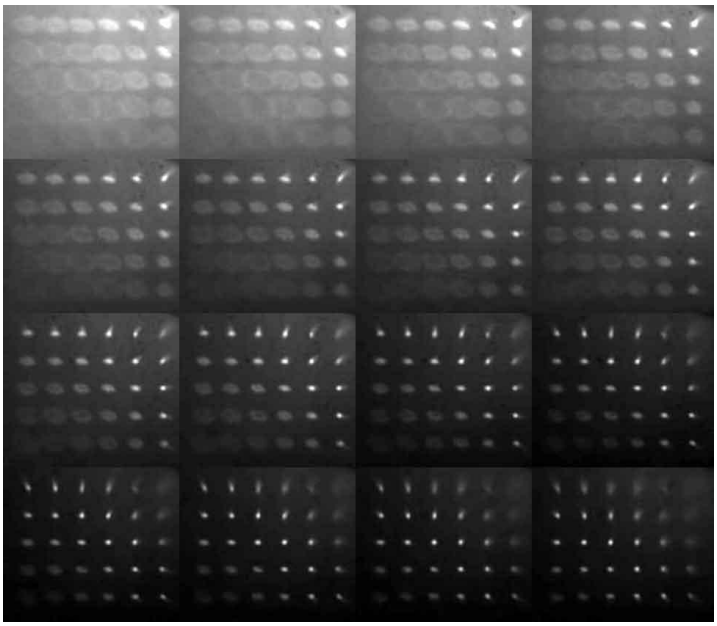

Figure 2.7: z-stack of a convex sample, Δz=1 µm (square size is 3x3 µm^2 at sample position, 50x objective).

System Modification for Lithography Thickness Monitor

The argon laser of the laser beam writer was replaced by a 405 nm laser diode. This type of laser allows us to work with H-line photoresists. As 405 nm lasers are used in consumer electronics (Blue ray disk players), they are cheap. Since the original Florod laser beam writer was designed to be used with an argon laser, some modifications were required in the optical elements. In addition preliminary experiments on the photoresist thickness monitor showed that the optical throughput of the alignment beam was too low to allow for the accurate determination of the photoresist film thickness from the reflection spectrum within a reasonable time frame (several milliseconds). More details on the thickness monitor is provided in reference [20]. To increase the optical throughput, the reflection and transmission spectra of all optical components of the laser beam writer were analyzed. The emphasis was on increasing the intensity of the white light alignment beam at the sample position, and to widen its spectral range. Several components (all mirrors) were replaced.

Spectrophotometry measurements were performed on all mirrors of Figure 2.2 using a Filmetrics F20 thin film measurement system. To calibrate the Filmetrics F20 system in transmission mode, two set points are entered in the software. The first set point is the reading of the receiver when there is a direct transfer of the light from emitter to receiver in the air. The second one is the reading of the receiver when there is a blockage between emitter and receiver. The first set point is considered as 1 and the second set point is considered as 0 in the software. In reflection mode, total reflection is defined as 1 and total blockage is defined as 0 reflection in the software. Tilted optical surfaces shift the beam direction and change the coupling of the receiver. So, the intensity

of the received beam may be higher than the maximum intensity found during the calibration procedure. In addition any small curvatures of the optical surfaces may also influence the coupling transmitter and receiver. Hence, in the F20 measurement results there are transmission or reflection values larger than 1, which of course have no physical meaning. For our purpose, it is only important to determine the shape of the reflection and transmission spectra. So, the variation of the transmission or reflection curves is more important than their absolute values.

The transmission and reflection spectra for mirror1 are shown in Figure 2.8. The data shows that mirror1 in transmittance mode works as a band-pass filter and has a transmission curve with a lot of structures. This filter in the original design of the machine is designed to block the laser beam to expose the eyepieces and camera. Because the laser alignment lamp (halogen lamp) is used during spectrophotometry for photoresist thickness measurement, this band-pass filter is not suitable in the new design of the system.

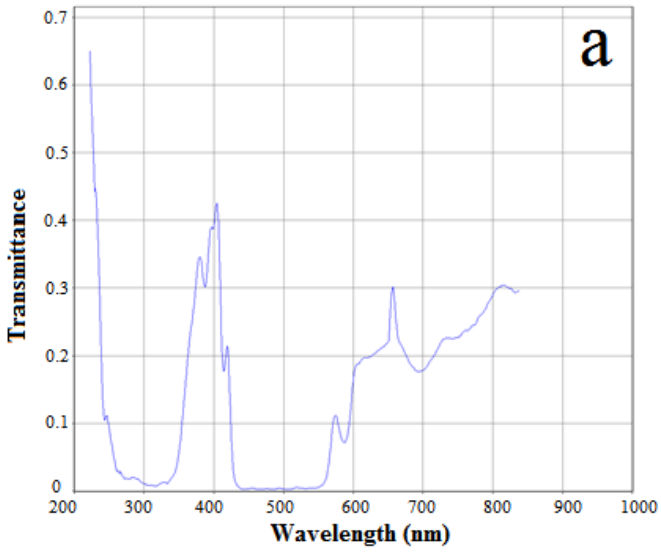

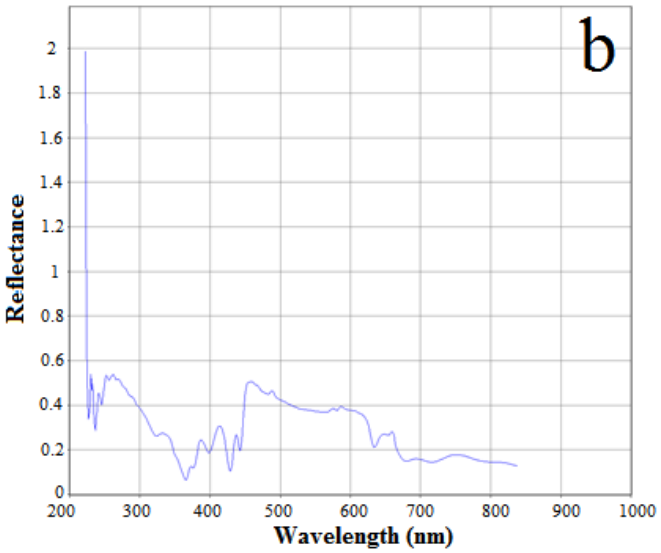

Figure 2.8: (a) Mirror1 transmittance, (b) Reflectance on surface B

To increase the optical throughput of the photoresist film thickness monitor and lower the transmission down to 500 nm, the original beamsplitter was replaced by a new beamsplitter with a smooth transmission curve that transmits wavelength down to below 400 nm (Edmund Optics elliptical beam splitter #48-915). The spectrophotometry measurement of the new beamsplitter are shown in Fig. 2.9.

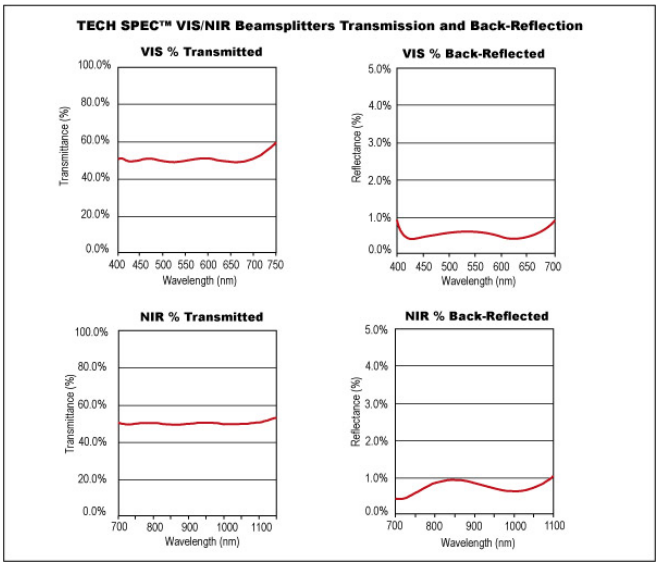

Figure 2.9: The new mirror1 transmittance and reflectance

http://www.edmundoptics.com/

A similar problem is also observed on mirror 5 as shown in figure 2.10.

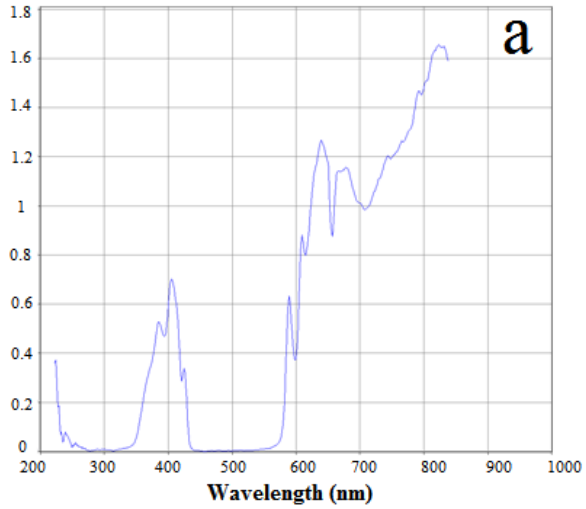

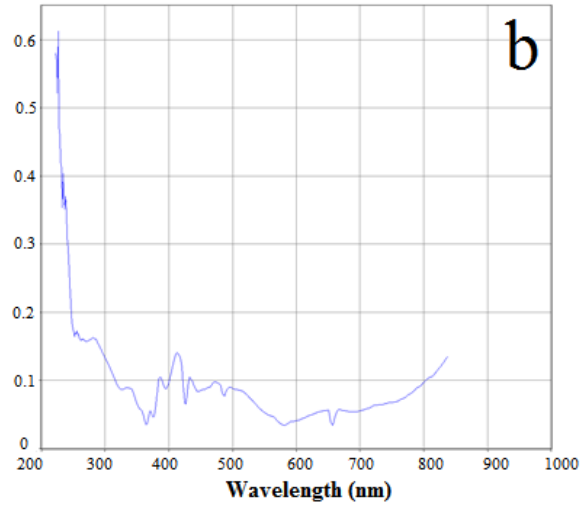

Figure 2.10: (a) The mirror5 transmittance (b) Reflectance on surface A

This mirror is also replaced with a new beamsplitter (Edmund Optics Plate beam splitter #32-363) with spectrophotometry measurement results shown in Figure 2.11.

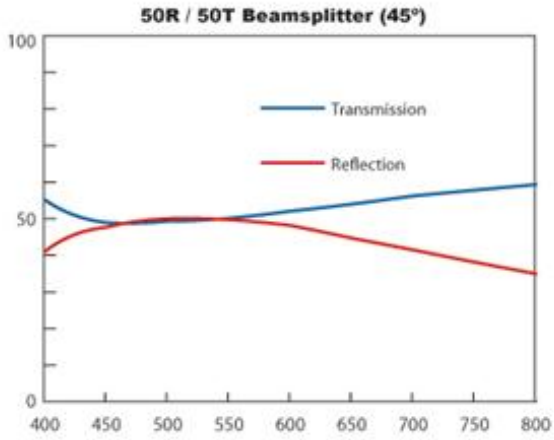

Figure 2.11: (a) The new mirror5 transmittance (b) Reflectance on surface A

http://www.edmundoptics.com/

The modifications described increased the optical throughput of the exposure/alignment beam column to allow for photoresist film thickness measurements, each 10 millisecond. More details can be found in [20].

SLM Installation

The spatial light modulator was coupled into the system via the alignment beam optical port of the system. To do this, lens 4 and the halogen lamp were temporarily removed and the SLM setup was installed on a stand outside the machine (Figure 2.12). Although, eventually the SLM needs to be coupled into the exposure/alignment beam via mirror 5, this approach gave us more flexibility and space.

The laser beam after being modified by the SLM passes through the entrance pupil of the laser beam writer. An intermediate image is formed at the position of the beam aperture. This intermediate image is focused on the sample by the laser beam lens (lens 3) and the objective.

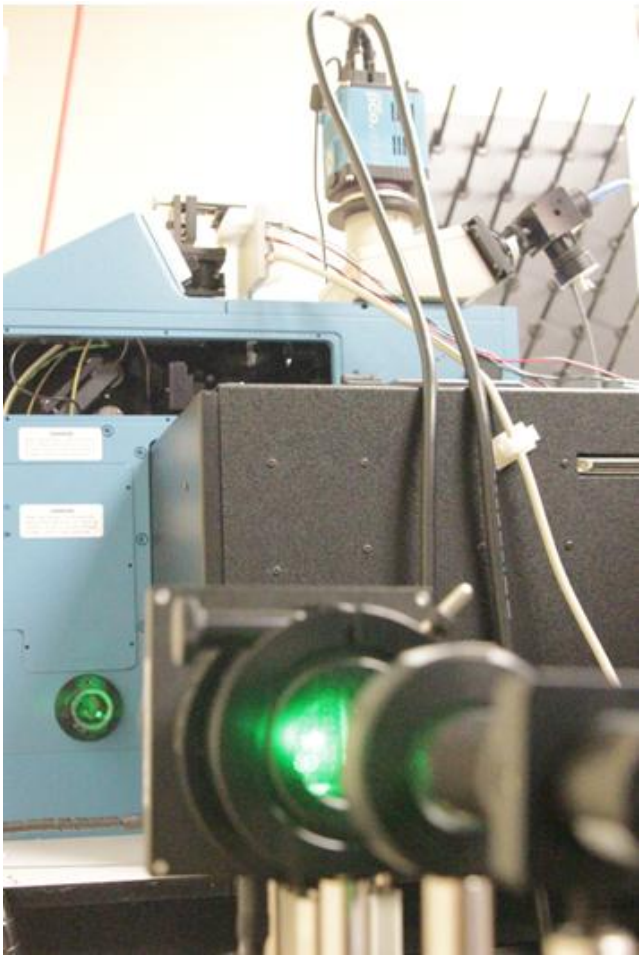

Figure 2.12: Entrance pupil modification for SLM installation

CHAPTER III: SPATIAL LIGHT MODULATOR

Three different techniques are presented in this thesis to shape the laser beam on a tilted or curved surface. All techniques are implemented on a phase Spatial Light Modulator (SLM). This chapter describes primary parameters of SLMs as the main device used in this research for the beam shaping. Two SLMs used in this study, the Holoeye-PLUTO and Holoeye-LC2002, are described. The chapter also contains descriptions of the setups used to test these two SLMs, one working in transmittance mode and the other working in reflective mode.

Spatial Light Modulator Basics

A Spatial Light Modulator (SLM) is a device that is capable of spatially manipulating the phase, amplitude, or polarization of a light beam. Each SLM device contains a matrix of pixels that each can be addressed via the interface electronics of the SLM. The phase shift, transmission, or polarization of each pixel can be independently controlled optically or electronically often via a graphics interface card in a computer. SLMs with different modulation mechanisms exist such as mechanical, magneto-opical [21], electro-optical, and thermal [22]. The modulation mechanism deals with an intermediate representation of information that interacts with the modulating medium

[23]. The modulators used for the work presented in this thesis are of the third type, so called Liquid Crystal SLM (LC-SLM). Three types of LC-SLMs are on the market: Twisted Nematic (TN) SLMs in which the orientation of the LC molecules differs between the entrance and the exit window of the cell in a helix-like structure, Parallel Aligned Nematic (PAN) SLMs in which the alignment of liquid crystals is parallel to the substrate, and Vertical Aligned Nematic (VAN) SLMs in which the alignment of liquid crystals is perpendicular to substrate [24].

Spatial light modulators can be fabricated based on translucent (LCD) or reflective (liquid crystal on silicon: LCOS) technology. In transmissive PAN LCDs, a conductive transparent oxide layer (often Indium Tin Oxide, i.e. ITO) and a light modulator material (Liquid Crystals) are sandwiched between two glass substrate layers. A liquid crystal consist of rod-like molecules that are long and rigid and have a permanent electric dipole moment. These molecules have a tendency to orient themselves in the same direction, called the director, and to line themselves up along micro-scratches in a rubbed glass plate. Because of their electric dipole moment liquid crystal molecules can be oriented by an externally applied electric field. Such electric field can be applied to the liquid crystal molecules by applying an electric potential across the ITO electrodes of each SLM pixel. In the absence of this electric field, the LC molecules' alignment is parallel to the glass substrates, parallel to the scratches in the rubbed glass substrates (Fig. 3.1a). After applying an electric field to the molecules, they tilt towards the optical axis of the SLM while keeping their parallel alignment with respect to each other as shown in figure 3.1b. So the orientation of the LC molecules in a certain pixel can be changed by applying an electric field to a pixel. The liquid crystal molecules are birefringent. This

means that their optical properties, specifically their refraction index, depend on their orientation with respect to the electric field of the electromagnetic wave. This is further explained in Figure 3.1. Assume that the incident light is linearly polarized in the vertical direction. If no electric field is applied to the pixel, the polarization direction of the incident EM-wave is parallel to the long axis of the liquid crystal molecules (Fig. 3.1 a) resulting in a certain refraction index, n. Now if one applies an electric field to the pixel, its liquid crystal molecules rotate towards the optical axis of the pixel (Fig. 3.1b), which changes the pixel's refraction index. A change in the refraction index also causes a change in the phase for the light passing through that particular pixel [25, 26, 28].

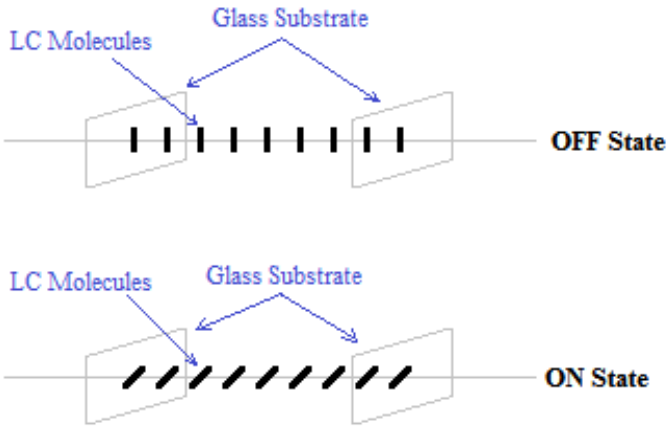

Figure 3.1: a: PAN LC molecules' alignment in the absence of electric field, b: PAN LC molecules' alignment after applying an electric field

In reflective LCOS SLMs each pixel consists of 7 major parts as shown in Figure 3.2: 1- cover glass with antireflection coating; 2- Indium Thin Oxide layer as an electrode; 3- LC layer; 4- alignment layer; 5- dielectric mirror; 6- aluminum electrode; 7- metal oxide semiconductor to address the pixel. [29]

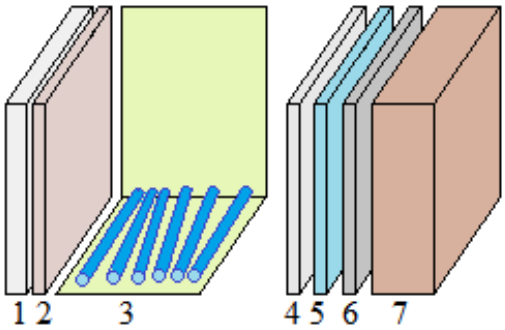

Figure 3.2: 7 major parts of each pixel on reflective LCOS SLMs

Phase modulation in reflective LCOS SLMs is similar to transmissive LCDs. Because in the reflective SLMs the light beam passes twice through the device, LCOS SLMs have a larger phase shift compared to transmissive LCDs with similar dimensions.

Twisted nematic LCDs consist of a liquid crystal material sandwiched between two glass plates that are covered by a transparent conductive oxide. The alignment layers on both sides of the cell are rubbed in perpendicular directions. For the cell of Figure 3.3 the liquid crystal molecules prefer to line up left-right at the top entrance window and front-back at the bottom exit window of the cell. This results in a 90 degrees twist of the director when moving through the cell from the entrance to the exit window. In the absence of an electric field, the LC molecules are in a 90 degree helix-like structure and their direction near the top entrance window is perpendicular to their direction near the bottom exit window. When polarized light enters the cell parallel to the liquid crystal molecules, the polarization will rotate while the light propagates through the material; the polarization will twist with the helix of the LC material. Applying an electric field to the liquid crystal molecules by applying an electric potential across its electrodes changes the

90 degree helix structure and orients the long axis of the liquid crystal molecules parallel to the optical axis of the cell (i.e. top down for Fig. 3.3). The optical properties of the cell are no longer anisotropic for light propagating along the optical axis of the cell, and the polarization direction of linearly polarized light traveling through the cell is no longer changed. By placing the cell between two crossed polarizers one can turn this polarization modulation into an intensity modulation. This is done in LC micro-displays and computer monitors. When the polarizers are not included in the device or when they are not crossed, the device will modulate also the phase or the polarization of the light

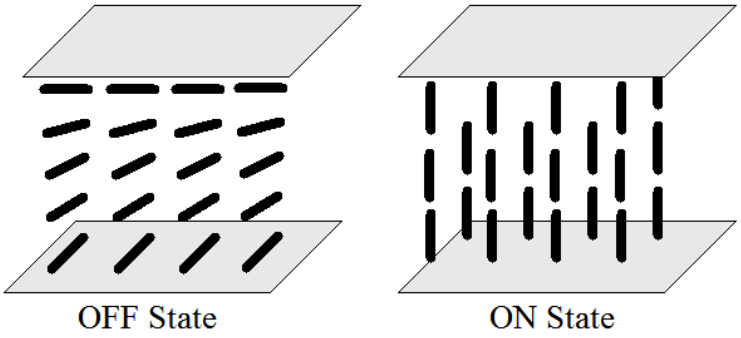

Figure 3.3: Twisted nematic LCD

The maximum phase change that can be obtained with a LC SLM depends on the birefringence of the liquid crystal molecules and on the thickness of the modulator. The birefringence of the liquid crystal molecules depends strongly on the wavelength, often increasing towards the shorter wavelength range. Thicker SLMs have a larger modulation depth, but they are also slower because more molecules need to be rotated. Thicker cells require larger electric potentials to rotate all liquid crystal molecules. Thicker cells also place a restriction on the maximum lateral resolution. Furthermore, for pixel dimensions

comparable to the pixel thickness, the electric field can no longer be considered to be constant throughout the cell thickness.

LC SLMs are essentially liquid crystal micro displays, and are inexpensive as they are mass produced and applied in consumer products as liquid crystal displays in cell phones, televisions, projectors, cameras and other electronics. The same chipsets that are used to control computer monitors and micro-displays can be used to load phase patterns in a LC SLM. Computer control of a SLM is easily implemented via the 2nd monitor port on the graphics card. Several companies currently sell the phase LC SLM (see Table 3.1). Most devices listed in Table 1 have a modulation depth of at least one period. The applied voltage to the electrodes of each pixel is quantized. Specified bit depth (BD) varies from 8 to 16 bits for various modulators that are on the market. Noise and fluctuations of the pixels' electrode voltages result in a realized bit depth between 6 to 10 bits for the devices listed in Table 3.1.

Table 3.1: Commercial Liquid Crystal Phase Modulators.

Company	#pixels	Pixel Size	# Bits
BNS	512x512	15x15um2	16
Holoeye	800x600	32x32um2	8
Holoeye Pluto	1920x1080	8x8um2	8
Meadow Lark	127 Hex	1x1mm2	
Hamamatsu	800x600	20x20um2	8
Jena Optics	640x1	3x100um2	12

SLMs Used in this Study

Two SLMs were used in this research: the LC 2002 transmissive phase and amplitude modulator SLM and the PLUTO reflective phase only spatial light modulator, both manufactured by Holoeye.

As shown in figure 3.4, LC 2002 is an 800 x 600 pixels resolution transmission mode twisted nematic SLM with a bit depth of 8 bit (256 levels). Pixel pitch of LC 2002 SLM is 32 μm and the maximum accessible phase shift is 2π. The device frame rate is 60 Hz and to address the pixels, a SVGA resolution 8 bit grayscale image should be uploaded via VGA port. The device has a fill factor of 55%, which means that only 55% of each pixel is transparent. The other area of each pixel contains the control electronics. Pixels have a thickness of 10 um. Light incident under larger angles of incidence will go through two different pixels.

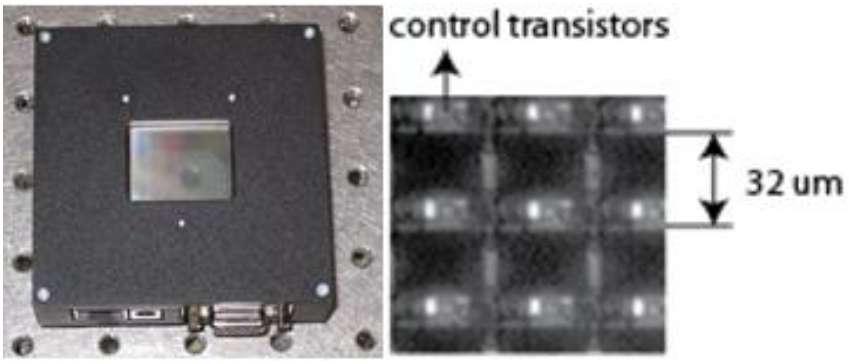

Figure 3.4: Holoeye Model-LC 2002 modulator (left) and optical image of pixel array (right)

The basic setup for the LC 2002 SLM is illustrated in Figure 3.5. It consists of a laser emitter, expansion lenses, and two polarizers one behind and one after the SLM.

Considering the Twisted Nematic structure of the LC 2002, to obtain phase-mostly modulation the polarizer in front of the SLM is not parallel or perpendicular to the alignment layers.

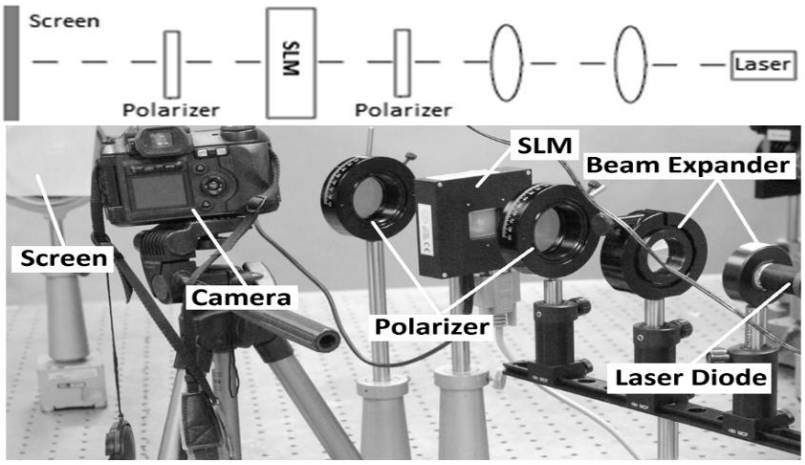

Figure 3.5: Basic setup for LC 2002 SLM

PLUTO (Fig. 3.6) is a reflective LCOS PAN-SLM and allows for pure phase modulation. It has an array of 1920 x 1080 pixels. Although the specification show a bit depth of 8 bit (256 levels), noise, drifts and thermal instabilities result in a realized bit depth not much more than 6 bits. The Pixel pitch of the modulator is 8 µm. The maximum accessible phase shift is 7.7π at 405 nm. The device frame rate is 60 Hz and to address the pixels a HDTV 8 bit grayscale image should be uploaded via a DVI port. The fill factor of the modulator is 87% which is considerably higher than the fill factor of the LC2002 and results in a larger optical throughput for Pluto. The control electronics of the Pluto SLM is integrated behind the pixel and not visible with normal optical microscopy.

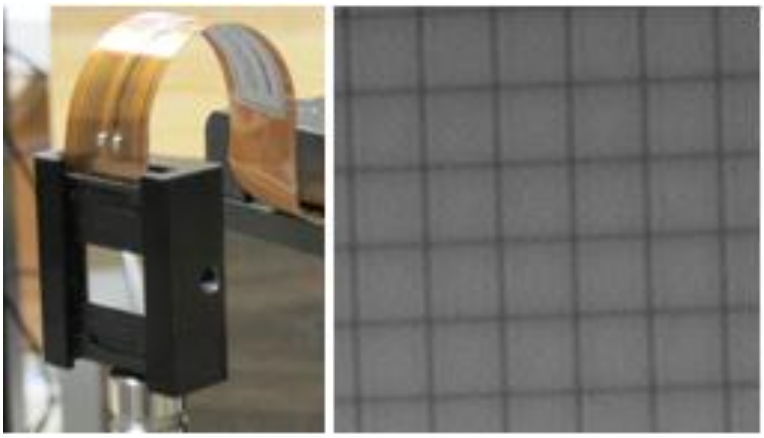

Figure 3.6: Holoeye PLUTO modulator (left) and optical image of pixel array (right).

The basic setup for the PLUTO SLM is illustrated in Figure 3.7 which consists of laser emitter, expansion lenses, a polarizer in front and behind the SLM, and a semi-transparent mirror (i.e. a beamsplitter). Note that in Figure 3.7 the modulator is positioned behind the beam splitter cube, and that the 2nd polarizer and projection screen are not included in the figure.

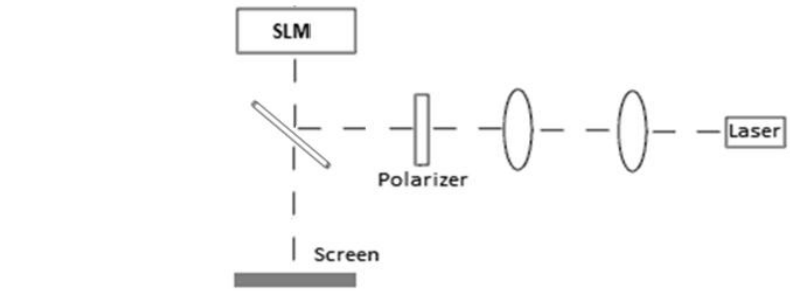

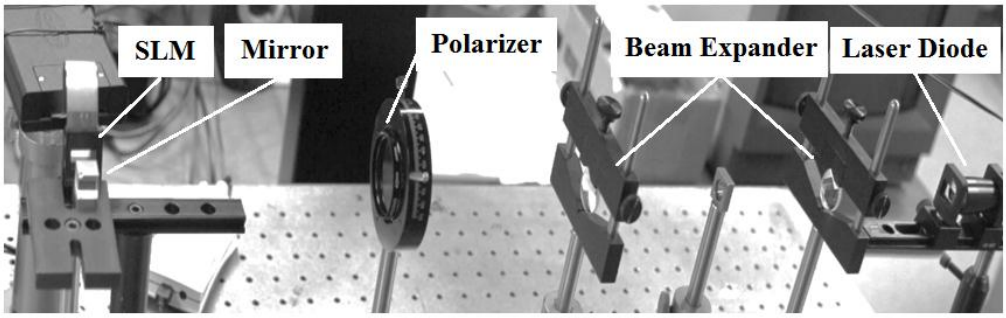

Figure 3.7: Basic setup for PLUTO SLM

In this research, all functions are first processed in LabView and Visual Basic. Then the generated images are used to address the SLMs using the Holoeye SLM Application Software.

CHAPTER IV: MULTI LENS TECHNIQUE FOR BEAM SHAPING

The depth of focus, DOF, is defined as a distance around the focal plane of a lens for which the image appears in focus. It is often defined in terms of the maximum allowable circle of confusion, C. As shown in Figure 4.1:

$$DOF = \frac{F/\#Cs_o{}^2}{f^2} = \frac{2Cs_o^2}{2rf} \qquad (4-1)$$

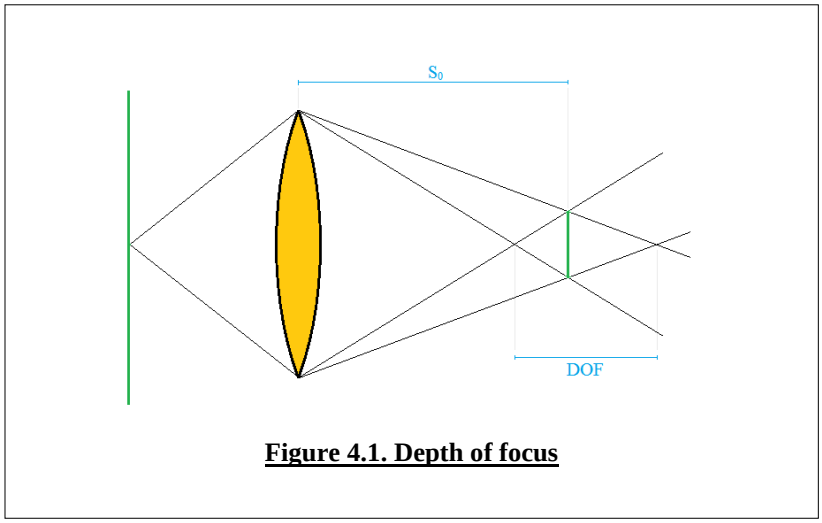

Figure 4.1. Depth of focus

where F/# is the f number, C is the allowed circle of confusion, S_o is the object distance, r is the lens diameter, and f is the focal length of the lens. The depth of focus is an important parameter when the image plane is not flat and it is perpendicular to the lens and object plane. Consider an object with a width d_w that is imaged on the image plane (see Fig. 4.2). If the image plane is tilted with angle θ, and $d_w\sin(\theta)$<DOF, the image is in-focus on the tilted plane.

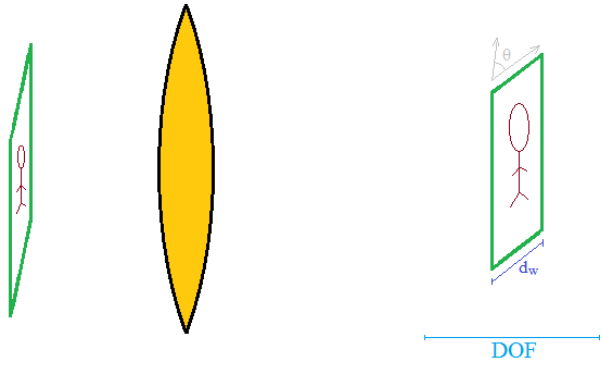

Figure 4.2. The image is in-focus on the tilted plane when $d_w\sin(\theta)<DOF$

As shown in Figure 4.3, when $d_w\sin(\theta)>DOF$, some parts of image are out of focus. A similar effects happens when the image plane is curved.

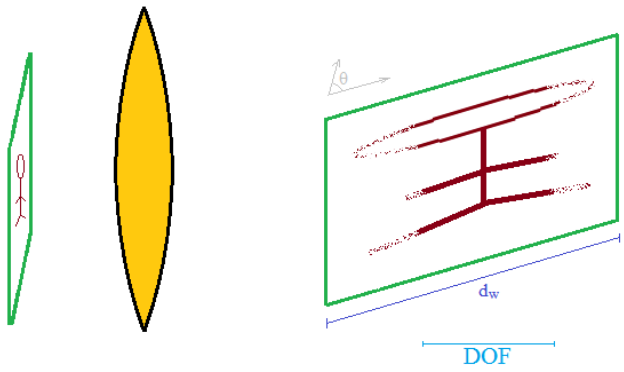

Figure 4.3. Some parts of image is out of focused on the tilted plane when $d_w\sin(\theta)>DOF$

To overcome this problem, one may design a system with two or more lenses with different focal lengths. The lens with the shorter focal length can focus the image on the left side of the image plane and the lens with the longer focal length can focus on the

right side of the plane (Fig. 4.4). In this way, the entire image is kept in-focus. In general, for a curved image plane, a multi lens array should be designed to keep each part of the surface in-focus. As the topography varies from sample to sample, the parameters of the multi-lens array need to be controllable by the setup.

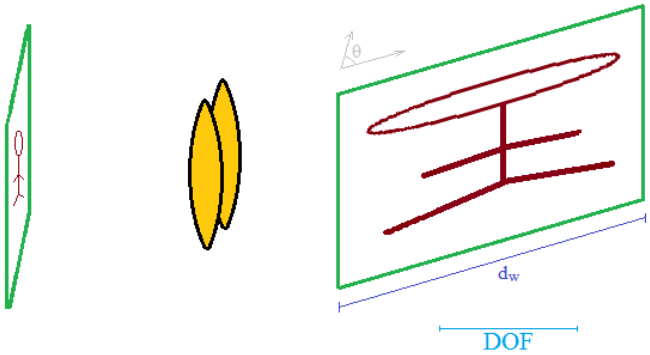

Figure 4.4. System with two lenses with different focal lengths

By implementing multiple lens functions in the SLM plane, one can create an array of beams to uniformly expose the photoresist material on a curved surface. To evaluate the performance and quality of the imaging of such a multi-lens array, a deep understanding of different errors affecting the quality of lenses implemented in a digital SLM is required. This chapter deals with this problem. First the phase function of a lens is defined. Then, the way a lens is build on a SLM is described. After that, the errors caused by a non-ideal lens function is evaluated mathematically. Finaly, the experimental results are presented and the limitations of using the multi lens technique to shape the beam on a non-flat substrate are discussed.

The Phase Function of a Lens Implemented on a LC SLM

An SLM can be used to create an optical refracting device such as a prism or a lens. To realize a converging lens in a SLM, the phase pattern image loaded in the SLM should be proportional to the thickness function of the lens [30]. A biconvex lens has a thickness distribution Δ(x,y) that is given by:

$$\Delta(x,y)=\Delta_o-R_1\left(1-\sqrt{1-\frac{x^2+y^2}{R_1^2}}\right)+R_2\left(1-\sqrt{1-\frac{x^2+y^2}{R_2^2}}\right) \quad (4\text{-}2)$$

where Δ_o is the lens thickness at the center between the two lens vertices, and R_1 and R_2 are the radii of surface curvature of the first and 2nd refracting surface. x and y are the distances from the optical axis in the x- and y-directions. The optical axis is the line that is perpendicular to the lens going through its center. For paraxial rays, the square roots in equation (4-2) can be replaced by their Taylor approximation, i.e. $\sqrt{1-x}=1-\frac{x}{2}$ resulting in [31]:

$$\Delta(x,y)=\Delta_o-\frac{x^2+y^2}{2}\left(\frac{1}{R_1}-\frac{1}{R_2}\right) \quad (4\text{-}3)$$

Assuming the lens refraction index is n_0 and assuming it is placed in air, the phase shift caused by the lens on a ray passing through lens position (x,y) is given by (in radians):

$$\phi(x,y)=\frac{2\pi}{\lambda}\left((n-1)\Delta_o-\frac{x^2+y^2}{2}(n-1)\left(\frac{1}{R_1}-\frac{1}{R_2}\right)\right) \quad (4\text{-}4)$$

Using the lensmaker's equation this can be written in terms of the focal distance f:

$$\phi(x,y)=\frac{2\pi}{\lambda}\left((n-1)\Delta_o-\frac{1}{2f}\left(x^2+y^2\right)\right) \qquad (4\text{-}5)$$

Which describes the phase function of a lens with focal distance f. Note that a lens described by equation (4-5) is no longer a spherical lens and has no spherical aberration for a point on the optical axis.

Instead of varying the thickness as a function of x and y, a lens can also be implemented by varying the refraction index and keeping the thickness constant. This kind of lenses are called Gradient Index (GRIN) Lenses. The refractive index profile of a GRIN Lens has the following form [32]

$$n^2 = n_0{}^2[1-(\alpha r)^2+\alpha_2(\alpha r)^4+\alpha_3(\alpha r)^6+\cdots] \qquad (4\text{-}6)$$

where α, α_2, α_3, are constants that define the focal length of the lens. Neglecting higher order terms and using the approximation of $\sqrt{1+x}=1+\frac{x}{2}$

$$n=n_o\left(1-0.5a^2\left(x^2+y^2\right)\right) \qquad (4\text{-}7)$$

The phase function realized by such GRIN lens is given by:

$$\phi(x,y)=\frac{2\pi}{\lambda}\left(n_o d-0.5a^2 n_o d\left(x^2+y^2\right)\right) \qquad (4\text{-}8)$$

Note that both equation (4-5) and (4-8) have the same position dependence. Furthermore note that the GRIN lens of equation (4-7) has also no spherical aberration. [33].

It is possible to implement such lenses in a phase LC-SLM since the refraction index of any pixel can be electronically controlled. Note that these lenses do not have

spherical aberrations but they have another type of aberration because their phase function are pixelated and quantized.

The relationship between the grayscale pixel value (GV) and the phase shift of a pixel is given by:

$$\phi(GV) = \frac{GV}{2^{BD}} MD = \frac{GV}{2^{BD}} d\Delta n \frac{2\pi}{\lambda} \qquad (4\text{-}9)$$

where BD is the bit depth of the SLM, MD is the modulation depth of the SLM (i.e. maximum phase shift), d is the thickness of a pixel along the SLM's optical axis, and Δn is the birefringence of the liquid crystal molecules. To implement a lens as described by equation (4-5) or (4-8) in the SLM, GV needs to be a function of the position:

$$GV(x,y) = \beta - \frac{\alpha}{PS^2}\left(x^2 + y^2\right) = \beta - \alpha\left(x'^2 + y'^2\right) \qquad (4\text{-}10)$$

Where PS is the pixel size, x' is the pixel column, and y' is the pixel row. x' and y' are defined with respect to the center pixel, i.e. assuming the pixel in the center of SLM has a row and column value of (0,0).

The phase function can now be calculated from equations (4-9) and (4-10):

$$\phi(x,y) = \frac{2\pi}{\lambda}\left(\frac{\beta\lambda MD}{2\pi 2^{BD}} - \frac{\alpha\lambda MD}{2\pi 2^{BD} PS^2}\left(x^2 + y^2\right)\right) = \frac{2\pi}{\lambda}\left(\beta\frac{d\Delta n}{2^{BD}} - \alpha\frac{d\Delta n}{2^{BD} PS^2}\left(x^2 + y^2\right)\right) \qquad (4\text{-}11)$$

Comparing equation (4-11) and (4-5) gives an expression for the focal length of a lens implemented in the LC-SLM:

$$f = \frac{2^{BD}\pi PS^2}{\alpha\lambda MD} \qquad (4\text{-}12)$$

A program was written in Visual Basic to calculate the gray scale image for a particular lens function. The input parameters of the program were α and β. The image pattern is then transferred to the LCD via a VGA port and a program written was in Labview 2011. In the rest of the chapter the lens function is investigated theoretically and experimentally.

Lenses Implemented in an SLM

In this study, the LC-2002 LC-SLM which has 800×600 pixels is used. The refraction index of each pixel can be controlled by loading the pixel with a gray-scale value between zero and 255. So, the pixel depth, BD, is 8 bits. The maximum diameter of a circular lens that can be implemented in the LC-2002 LC-SLM is 600 pixels or 19.2 mm. Although GV can be defined for all pixels of the SLM, i.e. $-400<x'\leq 400$ and $-300<y'\leq 300$, in the followings, only the pixels that have a distance $\sqrt{x'^2+y'^2} \leq 300$ from the center pixel of the SLM will be considered. So, the focus is on the performance of a lens with a circular entrance pupil.

Any value of GV(x', y') in the generated image is considered as an 8bit grayscale color. The grayscale image, after transferring to the LC-SLM, is translated into the corresponding phase function. The phase shift that the LC-SLM generates for minimum and maximum color values depends on its internal structure and can be calculated from equation (4-9). The focal length of the realized lens depends on α, and it can be calculated from equation (4-12).

To have a lens function which covers the whole area of the LC-SLM and that uses the full range of the BD, one should consider β=255 and $\alpha = \frac{255}{300^2} = 0.00283$ which makes the maximum grayscale value at the center of the LC-SLM and the minimum grayscale value near the edge of the lens. The generated image is shown in Figure 4.5. The pixel values outside the lens' entrance pupil are kept at zero. The corresponding focal length for the LC2002 at 532 nm following from equation (4-12) is very large and equal to 87.06 meters.

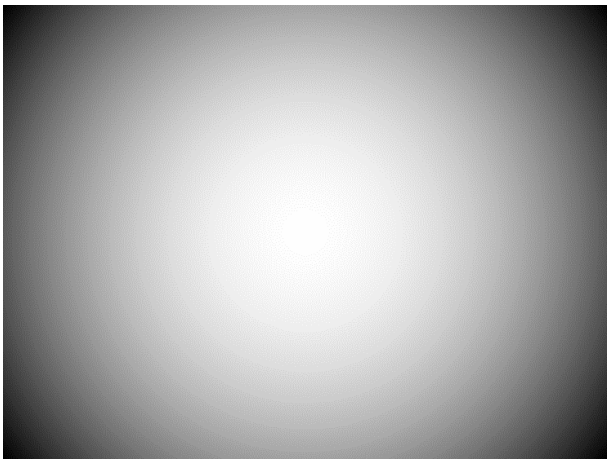

Figure 4.5: Phase Image of the lens function with n0=255 and α= 0.00283 (f=87.06m for LC-SLM at 532nm).

To have a better understanding of the phase distribution in the designed lens surface, the grayscale value along the x axis (y=0) of the LC-SLM is plotted in figure 4.6.

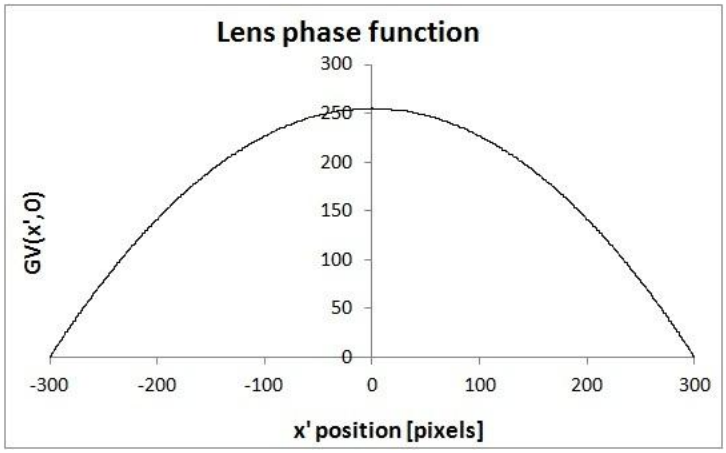

Figure 4.6: Grayscale value along the x axis of the lens function with β=256 and α= 0.00283 (f=87.06m for LC-SLM at 532nm).

It is possible to implement a lens with a shorter focal length in the LC-2002-SLM, but at the expense of the F/# of the lens:

$$f_{\min}(r) = \frac{\pi P S^2 r^2}{\lambda M D}$$
$$F/\#\big|_{f_{\min}} = \frac{\pi P S^2 r}{2\lambda M D} \qquad (4\text{-}13)$$

where r is the lens radius in pixels and the F/# is defined as f/(2r). Hence, the minimum focal length is proportional to r^2 and the f-number for the minimum focal distance is proportional to r. Figure 4.7 shows the minimum focal length and the corresponding F/# of lenses implemented in the LC-2002 and Pluto SLMs as a function of the lens radius r.

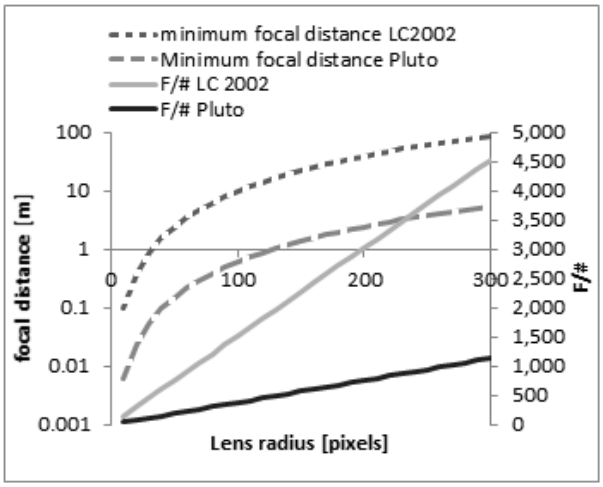

Figure 4.7: Minimum focal length and the corresponding F/# of lenses implemented in LC-2002 and Pluto as a function of the lens radius r

Since it is possible to make positive and negative lenses, the focal length of an SLM lens can be electronically changed across the range described by:

$$\frac{1}{\mathrm{f}_{\min}} \le \frac{1}{f} \le -\frac{1}{f_{\min}} \qquad (4\text{-}14)$$

Or in other words the electronic lens power range of the SLM lens is $2/\mathrm{f}_{\min}$. Assuming that the SLM lens is combined with the laser beam lens (lens 3 in Fig. 2.2) similarly as proposed in the paper of Takaki et al. [27], the focal length of the laser beam lens can be electronically altered to bring the sample in or out of focus. Assuming that the laser beam lens has a focal distance of f_r and that the distance between the laser beam lens and the SLM lens is zero, the electronic range of the effective focal distance of the compound lens, f, is given by:

$$\frac{1}{f_r} + \frac{1}{f_{\min}} \le \frac{1}{f} \le \frac{1}{f_r} - \frac{1}{f_{\min}} \qquad (4\text{-}15)$$

Lens 3 and the objective form an image of the beam aperture on the sample. Of course the image distance is a function of the focal length of the compound lens and can be calculated from the lens equation. Figure 4.8 below shows the depth of field range that can be electronically addressed by incorporating an SLM lens at distance 0 from laser beam lens 3 (Fig. 2.2) for the 50x objective. The horizontal line indicates the depth of focus of the 50x objective, i.e. 1.1 um. The use of the SLMs as electronic focusing devices is limited to lenses with a small radius. Lenses with a small radius however also have a small F/# resulting in a lower resolution. Assuming that the diameter of the compound lens is equal to two times the radius of the SLM lens, the focused laser spot size was estimated from the following expression:

$$D_{spot} = \frac{4\lambda f_{objective}}{\pi 2r} \qquad (4\text{-}16)$$

Or in other words the use of a small lens radius will result in a larger laser spot diameter: Less is used of the objective's lens pupil. The estimated diffraction limited laser spot size as a function of the SLM lens radius is plotted in Figure 4.9 together with the resolution of the objective (λ=532 nm; 50x objective). No effect on the system's diffraction limited spot size is expected for lenses diameters that cover the eye-pupil of the objective (i.e. 250 for Pluto and 63 for the LC2002). Figure 4.8 and 4.9 suggest that it is possible to increase the depth of field with a factor 5 by replacing the laser beam lens with an electronically controllable SLM compound lens and electronically controlling the focal distance to project different parts of the mask. Note that those lenses need to be implemented one after each other as each lens would require a diameter equal to the full eye-pupil of the objective. If the lenses are implemented parallel in a multi-lens array,

each lens will have a diameter smaller than the eye-pupil of the objective, and the diffraction limited spot size of the imaging system will be negatively influenced. Implementation of a multi-lens array instead of a single lens will increase the depth of field because of two effect: (1) the reduction of the lens diameter will increase the depth of field of each lens; (2) the ability to use different focal lengths for each of the lenses of the multi-lens array will increase the depth of field beyond that from a single smaller lens. The smaller lens diameters of the lenses in the multi-lens array however increase the diffraction limited spot size of the system.

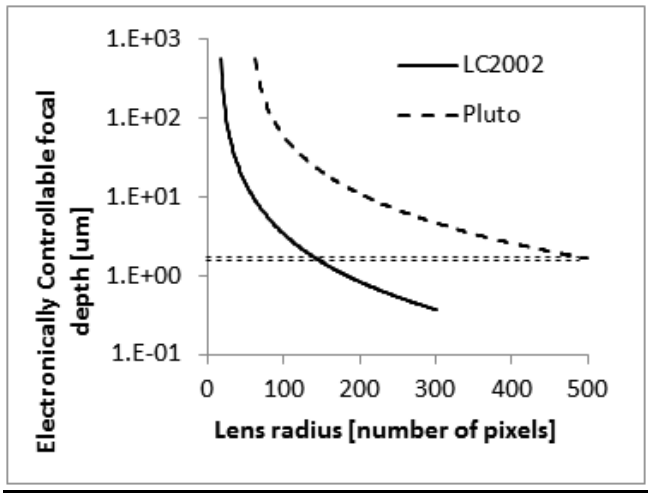

Figure 4.8: Electronically controllable focal depth for the LC2002 and Pluto together with the DOF of the 50x objective (50x objective, λ=532 nm)

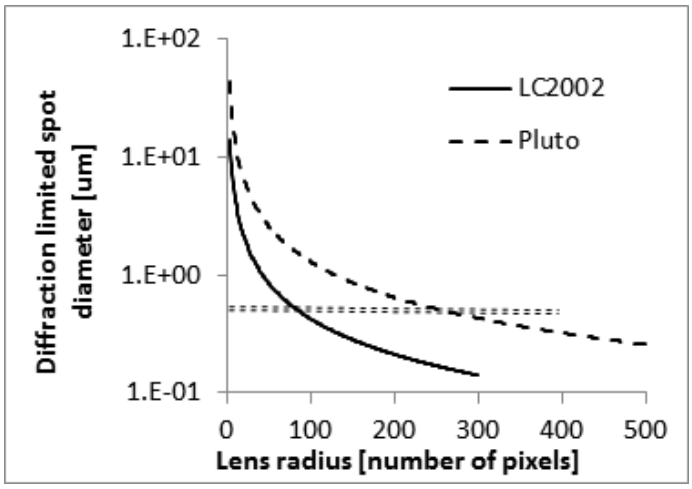

Figure 4.9: Diffraction limited spot size of focused laser beam together with system resolution without electronic focusing (50x objective, λ =532 nm)

Expansion of the electronically controllable DOF to a larger range requires SLM lenses with a larger focal distance. To implement stronger lenses, one can use a Fresnel lens approach: The light cannot see the difference between a 2π, 4π, or 6π phase shift, so it is possible to use the modulus function. Hence phase shifts ϕ that are larger than 2π can be implemented by loading the pixel with the gray scale value mod (ϕ,2π). This approach allows us to implement a GV function with an α value beyond $\frac{2^{BD}-1}{r^2}$.

The modulus function was implemented as follows:

$$GV(x',y') = \begin{cases} \beta-\alpha(x'^2+y'^2) & 0\le\beta-\alpha(x'^2+y'^2)<256 \\ \beta-\alpha(x'^2+y'^2)+256 & -256\le\beta-\alpha(x'^2+y'^2)<0 \\ \beta-\alpha\left(x'^2+y'^2\right)+512 & -512\le\beta-\alpha\left(x'^2+y'^2\right)<-256 \\ \vdots & \vdots \\ \beta-\alpha(x'^2+y'^2)+256k & -256k\le\beta-\alpha(x'^2+y'^2)<-256(k-1) \end{cases} \quad \text{(Eq. 4-17)}$$

Solving the boundaries for r≥0 gives:

$$GV(x',y') = \begin{cases} \beta-\alpha(x'^2+y'^2) & \sqrt{\frac{\beta-256}{\alpha}} \le x'^2+y'^2 < \sqrt{\frac{\beta}{\alpha}} \\ \beta-\alpha(x'^2+y'^2)+256 & \sqrt{\frac{\beta}{\alpha}} \le x'^2+y'^2 < \sqrt{\frac{\beta+256}{\alpha}} \\ \beta-\alpha\left(x'^2+y'^2\right)+512 & \sqrt{\frac{\beta+256}{\alpha}} \le x'^2+y'^2 < \sqrt{\frac{\beta+512}{\alpha}} \\ \vdots & \vdots \\ \beta-\alpha(x'^2+y'^2)+256k & \sqrt{\frac{\beta-256(k-1)}{\alpha}} \le x'^2+y'^2 < \sqrt{\frac{\beta+256k}{\alpha}} \end{cases} \quad \text{(Eq. 4-18)}$$

where k is the number of rings for the implemented Fresnel lens. Note that β does not influence the focusing power, but it just adds a constant phase factor. As an example, considering β=255 and α= 0.01 (f=24.64 m for the LC2002 at 532 nm) the function described in Eq.9 can be positioned in the pixel range of 800×600 up to k=9. This function is plotted in the Figure 4.10.

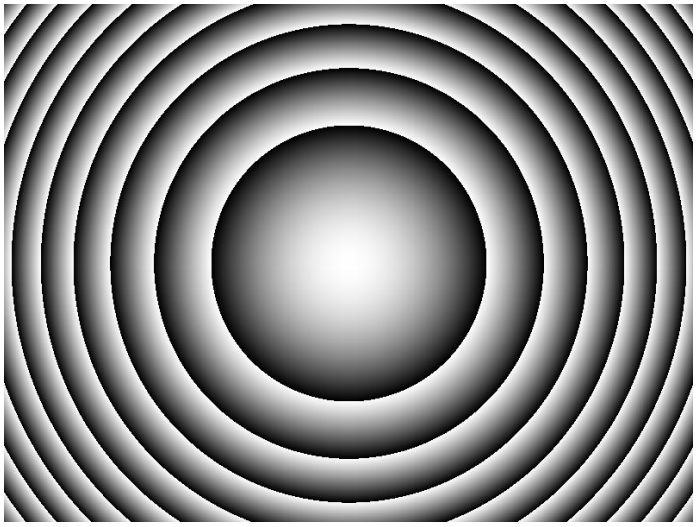

Figure 4.10. The phase image of the lens function with β=255 and α= 0.01 (f=24.64 m for the LC2002 at 532 nm)

The grayscale value along the x' axis (y'=0) of the LCD is plotted in Figure 4.11.

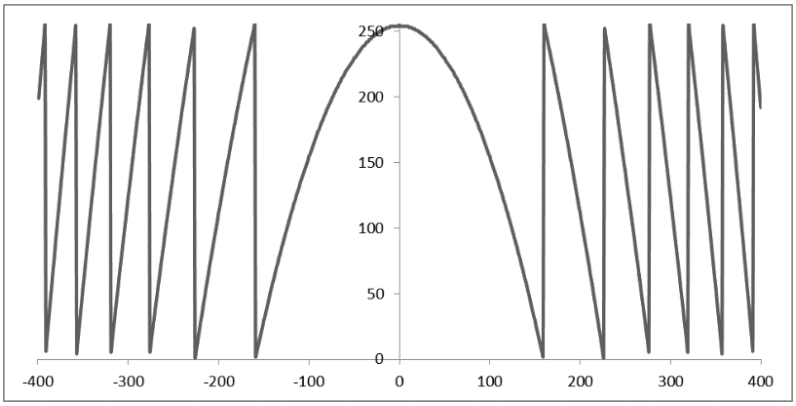

Figure 4.11: The grayscale value along the x axis of the lens function with β=255 and α= 0.01 (f=24.64 m for the LC2002 at 532 nm)

Note that the phase functions of both lenses, i.e. Figure 4.5, 4.6, 4.10, and 4.11, are pixelated and quantized. Figure 4.12a shows both the ideal phase function and its quantized-pixelated version for the lens of Figure 4.5. The difference between the phase function of the lens implemented on the SLM and the non-pixelated and non-quantized ideal lens phase function (see Fig. 4.12a) causes imperfect imaging, i.e. optical aberration. Figure 4.12b, Figure 4.12c and Figure 4.12d show the phase error caused by quantization, the effect of pixelation on the phase error, and the effect of both pixelation and quantization on the phase error respectively.

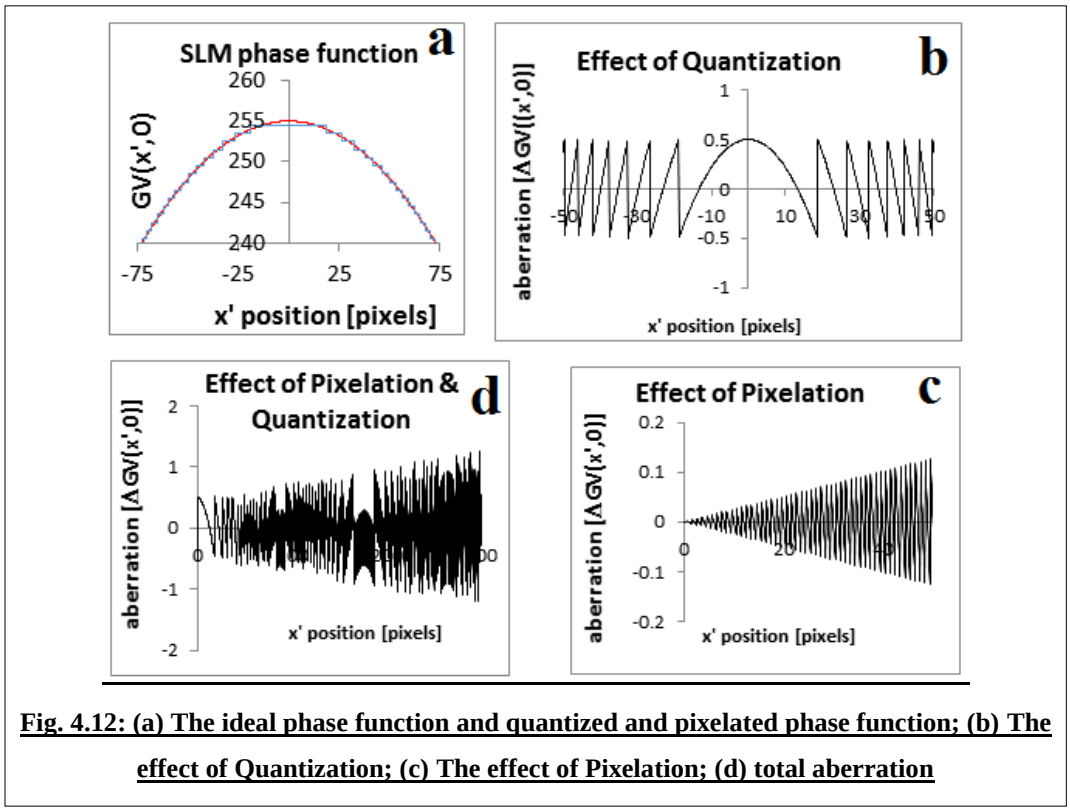

Fig. 4.12: (a) The ideal phase function and quantized and pixelated phase function; (b) The effect of Quantization; (c) The effect of Pixelation; (d) total aberration

Notice that the effect of quantization illustrated in Figure 4.12b, is to introduce a Fresnel lens with a different focal distance. Note that the Fresnel lens only expands $2\pi/256$. So, assuming parallel light entering the SLM, a portion of the light is focused in a different plane. Literature shows that multiple focal points have also been observed for Fresnel zone plates [35].

Figure 4.13 shows the grayscale image for a lens with a shorter focal distance (α=0.55, i.e. f= 44.8 cm at 532nm for the LC2002). It is clear from the figure that the quantized and pixelated version of the parabolic phase function is periodic; A multi-lens "array" is created rather than a simple lens. The difference between the parabolic and realized phase function is again caused by the quantization and the pixelation of the modulator. As shown in Figure 4.12b, the quantization error oscillates and its amplitude

is approximately constant across the exit pupil of the lens, i.e. +/- 0.5 a gray scale value. As the phase shift gradient is minimum at the center of the lens, the effect of quantization is maximum there. The effect of pixelation is zero on the optical axis but it is maximum near the edges of the lens as the phase shift gradient is maximum there and pixelation errors are proportional to the phase shift gradient. This is clearly illustrated in Figure 4.12c. For a parabolic phase function, the pixelation error is linear proportional to the distance to the optical axis. The pixelation error is also proportional to the pixel size, so, it decreases for higher resolution modulators.

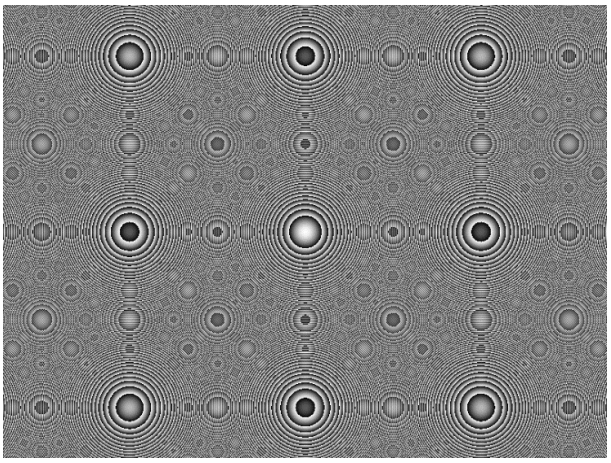

Figure 4.13. The phase image of the lens function with β =255 and α= 0.55 (f=0.448m for LC-SLM at 532nm)

In order to separate the effects pixelation and quantization have on the optical aberration the following definitions are made:

a. The pixelation aberration, $a_p(x',y')$, is the difference between the continuous lens function and the pixelated lens function, i.e.:

$$a_p(x',y') = \varphi(x',y') - Pixelated\left(\varphi(x',y')\right) \qquad (4\text{-}19)$$

b. The quantization aberration, $a_q(x',y')$, is the difference between the pixelated lens function and the quantized pixelated lens function, i.e.:

$$a_q(x',y') = Pixelated\left(\varphi(x',y')\right) - Quantized\left(Pixelated\left(\varphi(x',y')\right)\right) \quad (4\text{-}20)$$

Combining both equations gives:

$$Quantized\left(Pixelated\left(\varphi(x',y')\right)\right) = \varphi(x',y') - a_p(x',y') - a_q(x',y') \quad (4\text{-}21)$$

So with these definitions the total aberration is given by the sum of the two separate contributions, i.e. pixelation and quantization aberration:

$$a(x',y') = a_p(x',y') + a_q(x',y') \quad (4\text{-}22)$$

Figure 4.14 shows $a_p(x',y')$ and $a_q(x',y')$ of the lens implemented in Figure 4.5.

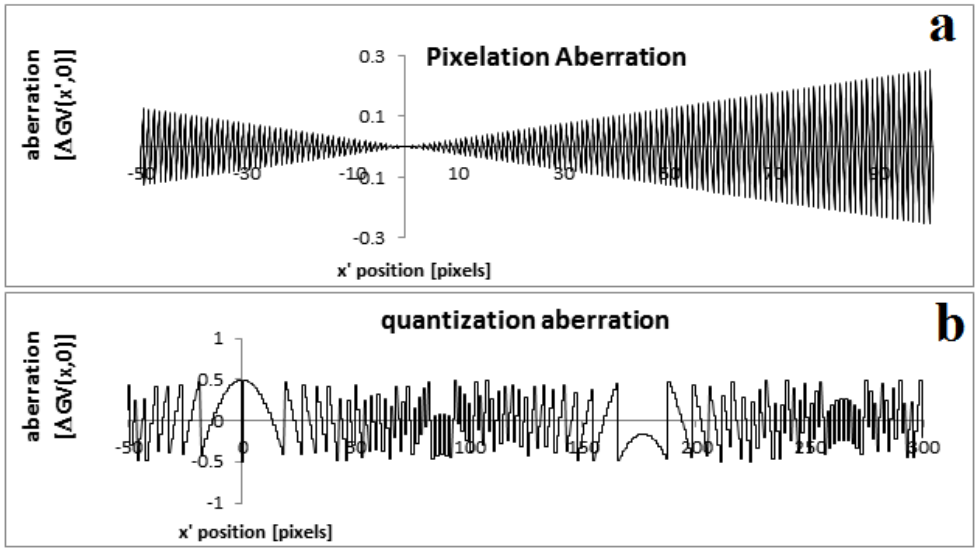

Fig. 4.14: (a) Pixelation and (b) quantization aberration of the SLM lens of Fig. 3.1.

The pixelation aberration, a_p, along the x' axis (i.e. y'=0) is a saw tooth function with a period equal to the pixel size and an amplitude that linearly increases from zero at the center to maximum near the edges of the lens. The quantization aberration, a_q, appears to be a Fresnel lens with a different focal distance. For larger values of α, a_q is a multi-lens array. More details on the aberration is provided in the next section.

It should be mentioned here that the effect of pixelation cannot be nullified by the implementation of a low pass filter as is often done in signal processing. The parabolic lens function has an infinite wide Fourier spectrum. From Fourier mathematics, it is known that the effect of pixelation (or sampling and hold) is to repeat the spectrum along the spatial frequency axis (diffraction pattern). As the non-sampled frequency spectrum has an infinite extent, pixelation will introduce distortion in the lower spatial frequency interval that cannot be removed by a simple low pass filter (read optical aperture centered around the optical axis).

As seen in Fig. 4.13 the lens function is repeated every $\frac{2^{BD}}{2\alpha}$. Therefore, considering α>0.32, the LC-2002 SLM generates more than one lens in the x axis. This fact is an important limitation that affects the minimum accessible focal length by any SLM while using the whole area of the SLM. As an example, α= 0.55 makes 9 major lenses in the area of the modulator which is shown in Figure 4.13. In addition the quantization, aberration creates weaker lenses between those main nine lenses sometimes referred to as ghost lenses. This is also clearly visible in Figure 4.14b.

The multi-lens effect of a quantized and pixelated Fresnel lens can be understood from the quasi-periodic character of the phase function. Figure 4.15 shows the phase

function of a Fresnel lens with α=0.00028. For small values of x, we see the parabolic function. For larger values of x the function consists of steeper segments of the same parabolic function. These segments are called quasi periods. As long as each quasi-period is sampled by two pixels, the local gradient of the phase function is realized, and light is bended towards a focal point on the optical axis [49]. Once the quasi-period is less than two pixels, aliasing causes a phase gradient with the wrong sign resulting in the EM wave being bent away rather than towards the optical axis. As the quasi-periods are minimum near the edge of the lens the maximum aperture radius of a lens can be calculated from the derivative of the phase function given in equation (4-10):

$$\Delta GV = 2^{BD} = \left.\frac{dGV}{dx}\right|_r \Delta x = -4\alpha x|_r 2 \Leftrightarrow r = \frac{2^{BD}}{4\alpha} \quad (4\text{-}23)$$

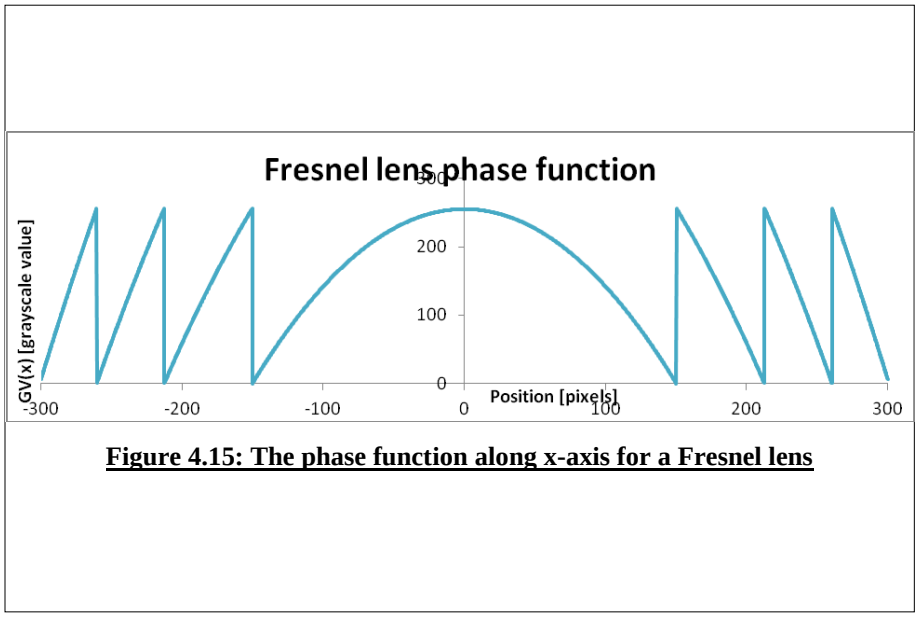

Figure 4.15: The phase function along x-axis for a Fresnel lens

Equation (4-12) can be used to rewrite this into expressions for f and F/# of the Fresnel lens:

$$f_{\min} = \frac{\pi PS^2}{\lambda MD} r$$
$$F/\#\big|_{f_{\min}} = \frac{\lambda MD}{\pi PS^2} \qquad (4\text{-}24)$$

Note that the F/# of a minimum focal distance Fresnel lens implemented in the LC-SLM is constant and independent of r (LC2002: F/15 and Pluto: F/3.9). Figure 4.16 shows how minimum focal distance and F/# at that f_{min} depend on r for the LC2002 and Pluto.

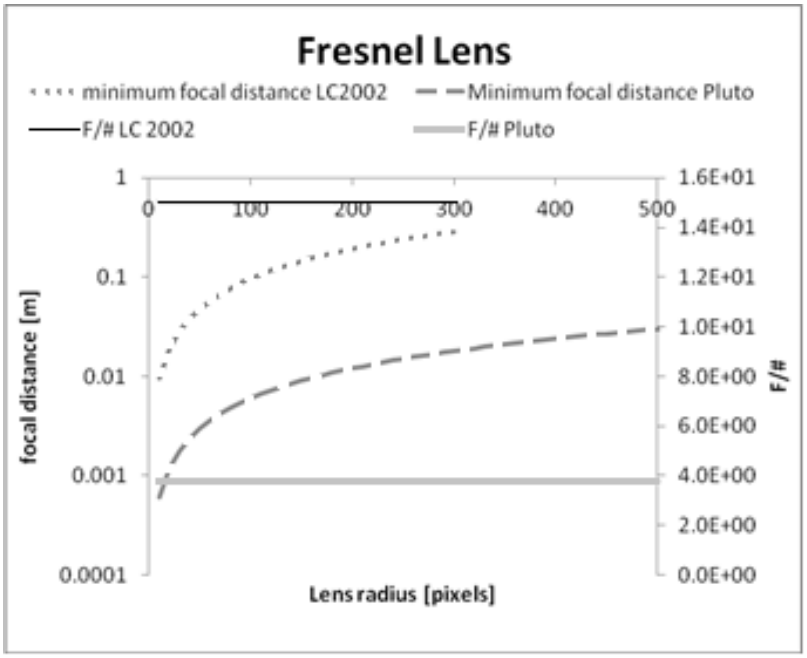

Figure 4. 16: Focal length and F/# as a function of radius for a Fresnel lens implemented in LC 2002 and Pluto

The content of Figure 4.16 was used to calculate the electronically controllable depth of focus for the Fresnel lens SLMs similar as shown above. A Fresnel SLM lens can extend the depth of focus of the system up to 16 mm when using Pluto and up to 0.7 mm when using the LC2002. The diffraction limited spot size dependency on the radius

of the lens is similar as for the non-Fresnel SLM lens. No impact on the diffraction limited spot size is expected for lens radii of 2 mm and above. This corresponds to the radius of the objective's eye-pupil (larger than 63 pixels for the LC2002 and larger than 250 pixels for Pluto).

Statistical Analysis on Pixelation and Quantization Aberration

As an example, for a lens with β=255 and α= 0.01, the calculated GV(x',y') value is an integer number in 12480 pixels of the LCD. It means that for this lens, the calculated GV(x',y') value is exactly equal to the specified grayscale value only in 2.6% of the pixels (P = 2.6%). Other 97.4% of the pixels are rounded to the nearest integer number. Figure 3.17 shows the difference between the pixels of this lens and the nearest integer. As illustrated in this figure, 52.6% of pixels are 0.25 off from the nearest integer number.

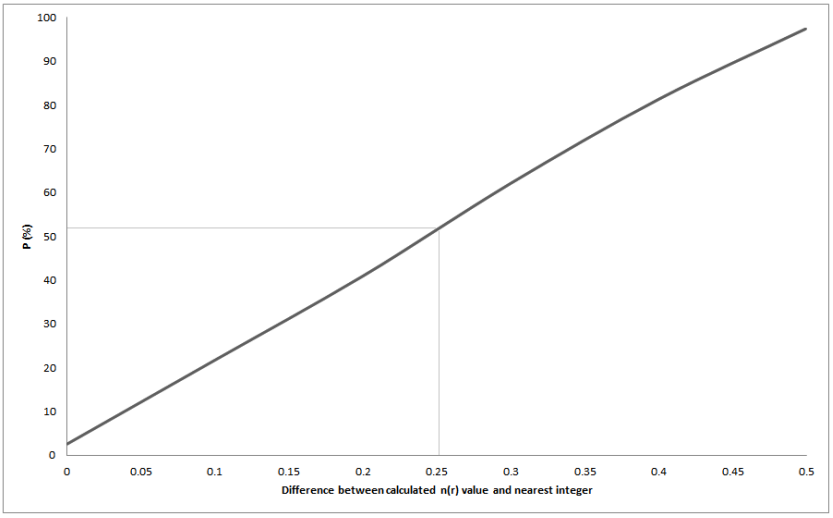

Figure 4.17. Percentage of the pixels vs. difference between calculated GV(x',y') value and nearest integer for a lens with β = 255 and α = 0.01 (f=24.64m for LC-SLM at 532nm)

The importance of the mentioned aberration is reflected clearly in Figure 4.18 which shows the percentage of the pixels that are 0.2 off from nearest integer for different lens parameters.

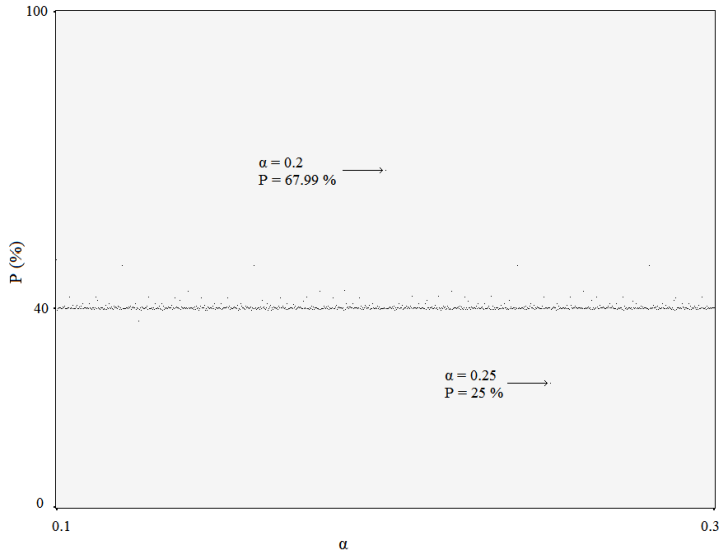

Figure 4.18. The P value for different α values from 0.1 to 0.3 (f=0.82m to 2.46m for LC-SLM at 532nm).

In this figure the value of α varies from 0.1 to 0.3 with the steps of 0.00025. The image clearly shows that the quality of the generated lens is affected by the focal length. Two examples are $\alpha = 0.2$ and $\alpha = 0.25$ as shown in the image. The quantization aberration of the generated lens with $\alpha = 0.25$ is larger than the lens with $\alpha = 0.2$. Recall that the quantization aberration has a significant effect on the center of the lens. Hence, for paraxial rays, a lens with $\alpha = 0.2$ has a better quality than a lens with $\alpha = 0.25$.

Statistical analysis of pixelation aberration gives a better idea about the lens quality because the magnitude of pixelation error is generally larger than the quantization error. To analyze the pixelation aberration, an array of 600X800 pixels is considered. Then the accurate value of the gray scale value of a lens with a specific α value is calculated at 100 points inside each pixel. The average of the differences between these 100 points and the gray scale value at the center of each pixel (δ) is calculated. This process is repeated for different α values from 0.1 to 0.32 with the steps of 0.00025 and plotted in figure 4.19.

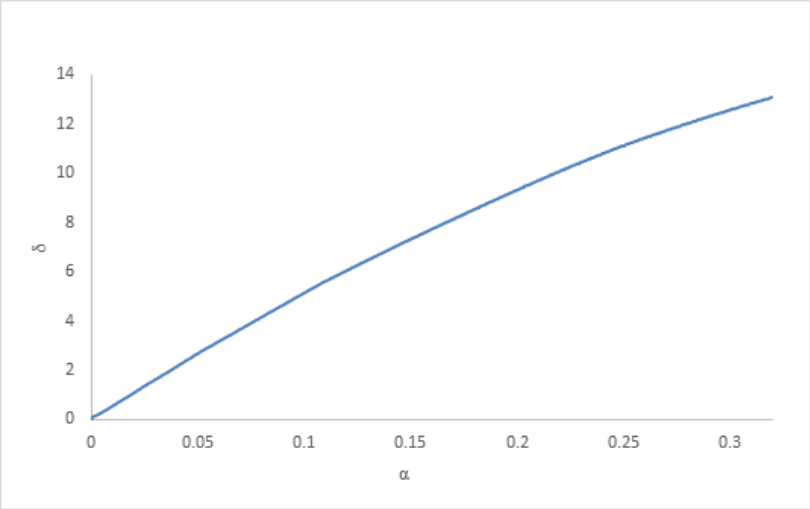

Figure 4.19. The average of the differences between GV of 100 points inside pixels and the GV at center of that pixel for different α

Figure 4.19 clearly shows that the pixelation aberration depends on the lens focal length. For shorter focal lengths, the error is larger. This is why because, pixelation errors are proportional to the phase shift gradient and phase shift gradient depends on α. Note that Fig. 4.19 is consistent with Fig. 4.14a.

Multi lens beam shaping

As shown in figure 4.20 two phase functions for two arrays of 600X400 are calculated for lenses with α=0.1 and α=0.12 (corresponding to f= 24.6 cm and f=20.5 cm at 532 nm for the LC2002).

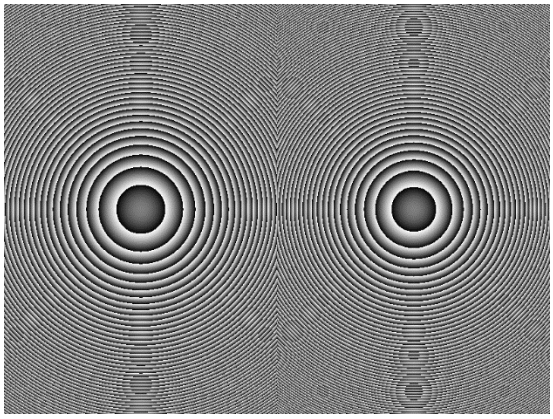

Figure 4.20. Left lens α=0.1 and right lens α=0.12

The dual lens phase function is used to focus an image on the tilted plane with tilting angle of about 65 degree. The result is shown in figure 4.21.

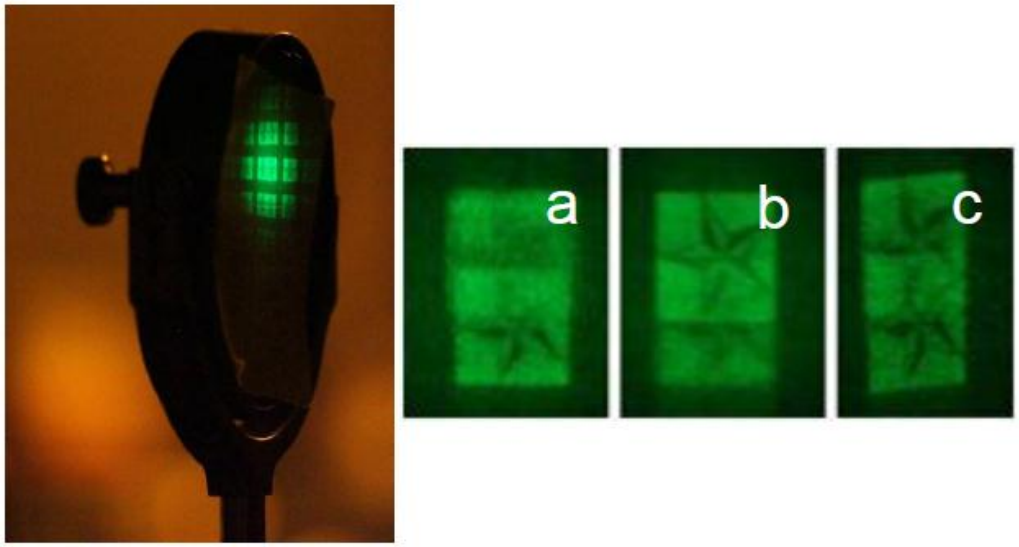

Figure 4.21. Projection of two Texas Lone Stars on a perpendicular (a, b) and a tilted surface (c) using dual lens phase function

Note that it is possible to implement 10 lenses that have a radius equal to the 50x objective's eye-pupil on Pluto and 39 lenses on the LC2002. This will allow for an extension of the depth of field with a factor 10x and 39x. Images generated with the LC2002 will have a poorer quality because of larger aberration.

Splitting the SLM into several regions to make a multi-lens array reduces the number of pixels used for each lens function. In this case, analysis of pixelation and quantization aberration provides a better knowledge about the image quality. Figure 4.22 illustrates the pixelation error for three different lens sizes: 800X600, 400X300, and 200X150.

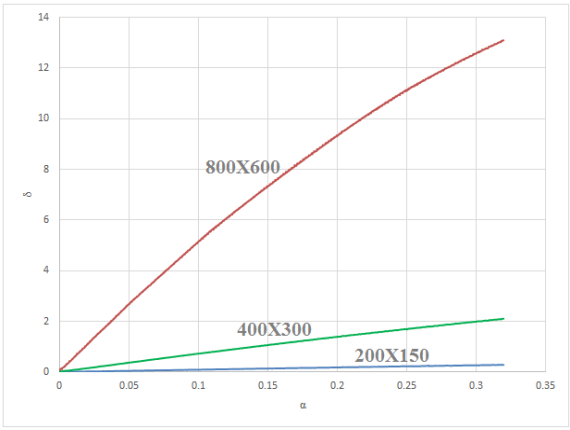

Figure 4.22. Pixelation error for three different lens sizes

This result shows that using less number of pixels significantly improves the quality of the lens assuming that one keeps the same focal distance. It confirms the facts discussed before. This is why because the pixelation aberration increases at the edge of

the lens: reducing the number of pixels cut the edges and reduces the pixelation aberration.

However, by having a very small size lens the quantization aberration becomes more important. For a very small size lens, pixelation aberration is close to zero and neglectable. But, the quantization aberration which has a magnitude from 0 to 0.5 affects the quality because the gray scale value is also very small near the center of the lens.

In addition to aberration a smaller size lens increases the depth of field as the numerical aperture of the system decreases (see equation 4-1). A smaller numerical aperture also decreases the optical resolution of the system. The minimum spot diameter of a laser beam focused by a microscope objective is proportional to the focal distance of the lens and inversely proportional to the lens' diameter (see equation (4-16) [36])

Therefore, lenses implemented on the SLM with a small diameter have a large minimum spot size due to diffraction. Their pixilation aberration is small and they are diffraction limited. SLM lenses with a large diameter have a negligible diffraction but a large pixelation aberration and their performance is aberration limited. An expression about the way the pixelation aberration influences the minimum spot size is currently lacking and should be the subject of further studies. However, preliminary experiments have shown that using the multi lens array function on the SLM to focus on a curved surface with detailed surface topography cannot give a very good result. It is currently not clear why and a more systematic investigation that includes the effect of topography on imaging quality need to be done. For the tilted surface or the curves that may be approximated by several simple step functions, the multi lens functions works very well.

CHAPTER V: TILTED LENS TECHNIQUE FOR BEAM SHAPING

Tilted lenses and lenses with a curved depth of focus are used in photography to emphasize certain aspects of the scenery. Additionally, a tilted lens can correct the out-of-focus effect of a tilted object in the laser beam writer because by tilting the camera plane with respect to the lens plane, the focal plane also tilts. In this chapter the use of a spatial light modulator to implement a tilted lens function is explained.

The chapter starts by describing different planes of an ordinary camera. Then, the Scheimpflug and Hinge principle are presented. The chapter focuses on the phase function of a tilted lens and describes a method to build a tilted lens using an SLM. The phase function of a tilted lens is loaded on the SLM and used to project an image on a tilted projection plane. Experimental results are presented to show how this approach can improve imaging on a tilted projection plane.

Scheimpflug Principle

The optical diagram of an ordinary camera as shown in figure 5.1 consists of three parallel planes: Film plane, lens plane, and the plane of sharp focus. Based on the lens parameters, distances between these planes are defined in a way that any object positioned in the plane of sharp focus is imaged sharply in the film plane.

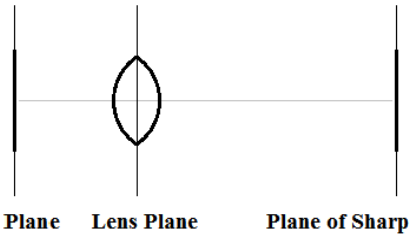

Figure 5.1: The diagram of an ordinary camera with three parallel planes

If the film plane and the lens plane are not parallel, their intersection is a line. Based on the Scheimpflug Principle [37], the plane of sharp focus also passes through that intersection line that is called Scheimpflug line as shown in Figure 5.2.

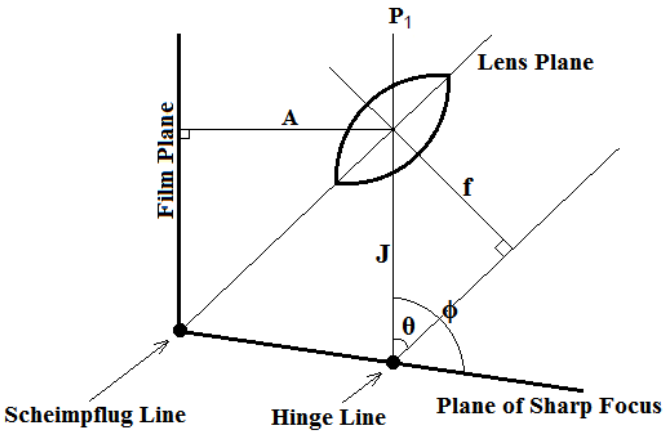

Figure 5.2: The diagram of a tilted lens, Scheimpflug & Hinge principle

where θ is the tilting angle of the lens, ϕ is the angle between film plane and the plane of sharp focus, and f is the focal length of the lens that defines the front focal plane. P_1 is a plane that passes through the center of the lens and is parallel to the Film plane.

The hinge rule states that P_1, front focal plane, and the plane of sharp focus intersect at a line called Hinge Line [37]. The Hinge rule is best understood by realizing that the points on the Hinge line are conjugate to points in the Film plane at infinity since they are at a distance of f from the lens. Based on the Hinge rule, knowing the film plane and lens tilting angle, we can find the distance of the hinge line from the lens' center (see Fig. 5.2):

$$J = \frac{f}{\sin\theta} \qquad (5-1)$$

The Scheimpflug principle also defines the relationship between the lens tilting angle and the angle between film plane and the plane of sharp focus:

$$\phi = 90^{\circ} + tan^{-1}\left[\frac{f}{A\sin\theta} - \frac{1}{\tan\theta}\right] \qquad (5-2)$$

where the distance between P_1 and film plane, A, and the lens tilting angle, θ, and the lens focal length, f, determine the angle between the plane of sharp focus and film plane, ϕ. Combining the Hinge rule and Scheimpflug principle together, all geometrical information about tilted lens imaging are found. Having A, f, and α; J, and ϕ can be calculated from equation 5-1, 5-2. Knowing the film plane, J, and ϕ, the plane of sharp focus can be defined.

To build the tilted lens function using a SLM the phase function of a tilted lens should be known. For a spherical thin lens positioned in the x-y plane and for paraxial rays, the phase shift introduced by the lens can be approximated by [31]:

$$\phi(x,y) = \phi_0 - \frac{\pi}{\lambda f}[x^2 + y^2] \qquad (5-3)$$

Tilting the lens under an angle of θ degrees with respect to x axis (axis perpendicular to the film plane), the new coordinates of the lens are defined as (x', y') where: x'= x cos(θ), y'= y. Substitute the new values in the phase equation [31] gives:

$$\phi(x', y') = \phi_0 - \frac{\pi}{\lambda f}\left[\left(\frac{x'}{\cos\theta}\right)^2 + y'^2\right] \qquad (5-4)$$

The equation 5-4 is then generated on the SLM and a real object is used for experimental tests. Figure 5.3 illustrates the system setup to investigate the results of the tilted lens function. Figure 5.3a shows the optical diagram of the setup that consists of a mirror to increase the distance between the object and the SLM. Using two polarizers, the Pluto SLM works in the pure phase modulation mode (Fig. 5.3b). A grid is used as a real object in this experiment (Fig. 5.3c). The SLM has only a tilted lens phase function (Fig. 5.3d). The results are observed with the system's camera when a level flat sample is placed on the xy-table or a tilted sample is placed on the xy table. (Fig. 5.3e).

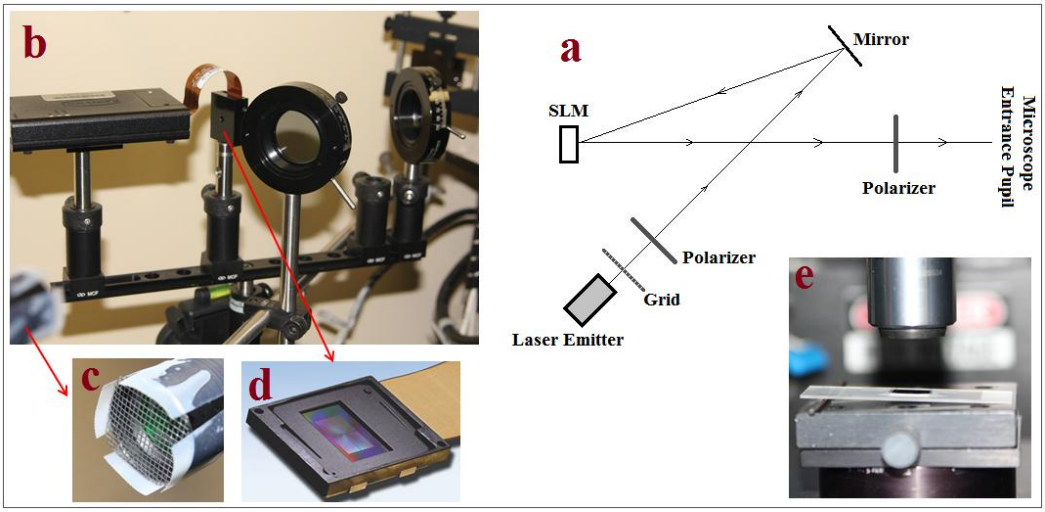

Figure 5.3: The system setup to investigate the results of tilted lens function

Figure 5.4 shows the grid structure under the microscope when using a normal (non-tilted) lens function. The sample is tilted with an angle of 1.76^0 and a 20x objective lens (Mitutoyo 378-804-2, 20X, N.A. = 0.42) is used in this experiment. The z-stage on the microscope is adjusted in a way to keep the left side of the image in-focus (Fig. 5.4b). As shown in Figure 5.4c the right side of the sample is out of focus.

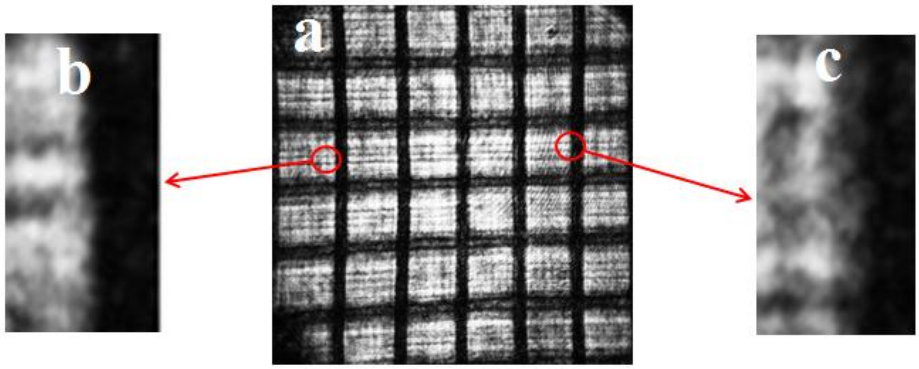

Figure 5.4: Tilted sample ($\theta=1.76^0$), flat lens, 20x objective, 19.5x36.7 µm2, Z= 0µm

Moving the z-stage 11µm, the focal point of the image shifts from left side of the image to the right side (Fig. 5.5a). Figure 5.5b shows out of focusing on the left side of the sample and Figure 5.5c shows in-focus on the right side.

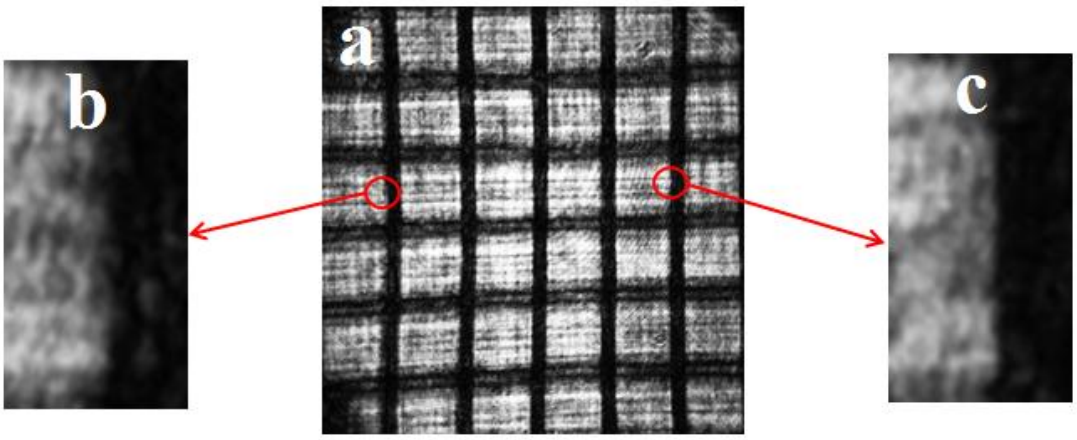

Figure 5.5: Tilted sample (θ=1.76^0), flat lens, 20x objective, 19.5x36.7 µm2, Z= 11µm

In the second experiment all parameters are the same as in the first experiment but the lens function is a tilted lens with a tilting angle of 27.5^0. Figure 5.6a shows the sample when the z stage is adjusted at the origin. The left side of the sample is in-focus (Fig. 5.6b) and the right side is out of focus (Fig. 5.6c).

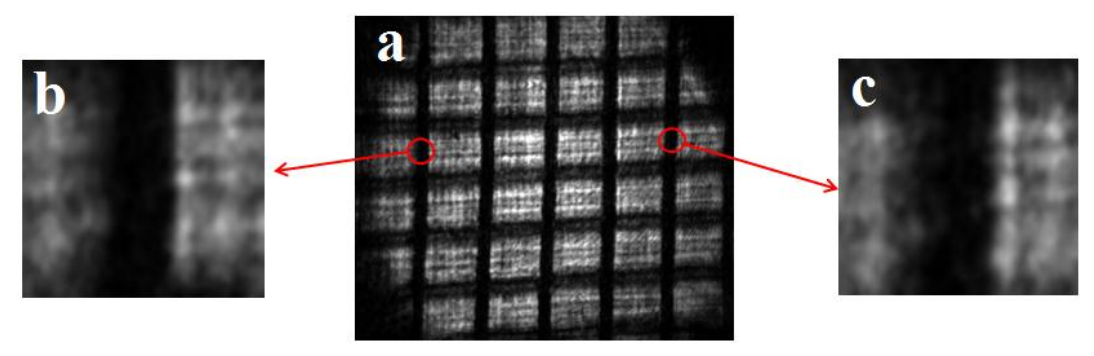

Figure 5.6: Tilted sample (θ=1.76 ^{0}), tilted lens (θ=27.5 ^{0}), 20x objective, 25x25 µm2, Z= 0µm

A 3µm movement in the z-stage shifts the focal point to the right side of the sample as shown in Figure 5.7: where the left side is out of focus (Fig. 5.7b) and the right side is in-focus (Fig. 5.7c).

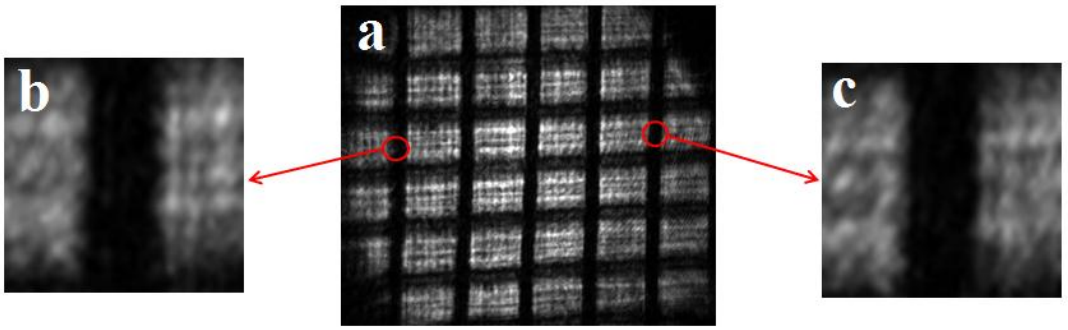

Figure 5.7: Tilted sample (θ=1.76 ^{0}), tilted lens (θ=27.5 ^{0}), 20x objective, 25x25 µm2, Z= 3µm

The 3µm movement in the z-stage position shifts the focusing from the left to the right side of the sample when using a tilted lens. In comparison an 11µm movement is required when using a non-tilted lens. This shows that the tilted lens corrects the imaging for the tilted sample. Note that the results in this chapter were obtained by using a real object. It was observed during the experiment that an SLM lens behaves poorly compared to a conventional lens when the incident light is not perpendicular to its surface. It is currently not clear why. Also papers and reports that show results of imaging of real objects with SLM lenses are scarce. It is recommended that the experiments of this chapter are repeated with a setup where the tilted SLM lens is replaced by a compound lens. The compound lens should make sure that the light incident on the SLM lens is perpendicular to its surface.

CHAPTER VI: DIRECT DIFFRACTION TECHNIQUE FOR BEAM SHAPING

Diffraction theory can be applied to realize an intensity distribution on a distant projection screen using a phase SLM. This is well known and currently investigated by various projector manufacturers as a more energy efficient projection technology. As shown in figure 6.1, a phase distribution on the SLM plane is diffracted by a uniform amplitude incident beam to form an image on the projection plane. A modified version of this technology could be used to project an image on a tilted or curved surface. This chapter discusses methods on how the standard lens-less projection techniques can be used to improve imaging on inclined and curved susbstrates.

The chapter, starts with decribing the diffraction theory between parallel planes oriented perpendicular to the system's optical axis. Then the diffraction equations for diffraction between two non-parallel planes are derived from the standard Fresnel diffraction equations.

Next the inverse phase problem is introduced: how to find the phase distribution in the SLM plane that creates a certain intensity distribution on the diffraction pattern. In literature several different algorithms have been proposed to solve this problem. In this thesis the iterative Gerchberg Saxton algorithm is used. The Gerchberg Saxton algorithm was implemented in Visual basic for three different configurations i.e. (1) Fraunhofer diffraction; (2) Fresnel diffraction on a projection plane at finite distance; (3) Fresnel

diffraction on an inclined surface at finite distance. The algorithm was used to calculate the SLM phase function to create a test pattern on a tilted distant projection screen.

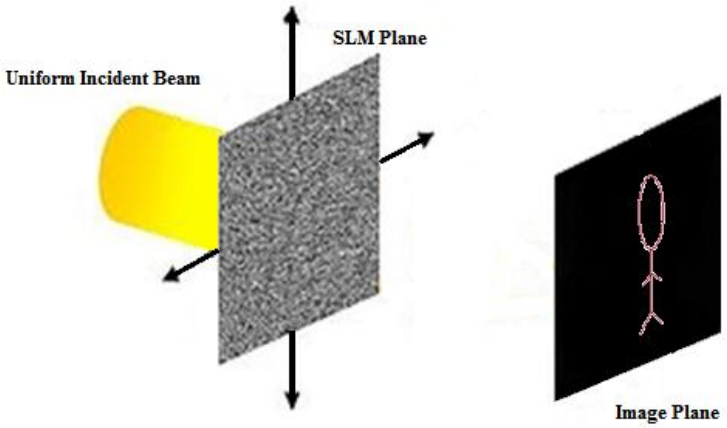

Figure 6.1: Diffraction between two parallel planes

Diffraction

Sommerfeld defined diffraction as any deviation of light from rectilinear paths which cannot be interpreted by refraction or reflection. Starting from Maxwell's equations and using the theory of Green's functions, Sommerfeld derived a relationship to calculate the diffraction pattern caused by an opening in a perfect conducting semi-infinite planar screen (x,y,0) on a projection screen (u, v) placed at a distance of w from the diffracting screen. It relates the optical fields in both planes. Although Sommerfeld's derivation ignored the vector character of the light, it is shown to be a good

approximation as long as the dimensions of the features on the planar diffracting screen are much larger than the wavelength of the used light and the angles of light are small compared to the optical axis of the system [39, 31].

Since the dimensions of a pixel of the SLM are approximately 30x larger than the wavelength of the used light, the use of a scalar diffraction model is justified. Based on the Rayleigh-Sommerfeld diffraction integral a distribution like E in the x-y plane is diffracted into an electric field distribution E_d in the u-v plane (u,v) positioned at a distance of w from the diffracting screen. If the projection screen is not perpendicular to the optical axis of the system, w varies across the projection screen, and Ed is a function of u, v, and w, as shown in Figure 6.2:

$$E_d(u,v,w) = \frac{1}{2\pi}\iint E(x,y,0) \times \frac{e^{-ikr}}{r} \times \frac{z}{r} \times \left(ik + \frac{1}{r}\right) dxdy \qquad (6-1)$$

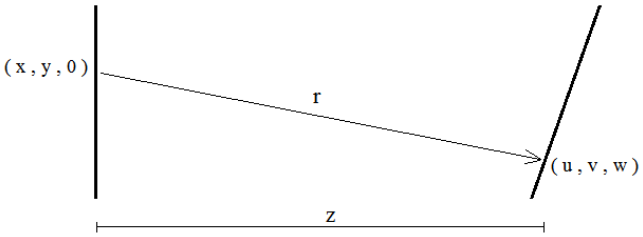

Figure 6.2: Diffraction geometry

where:

$$r = \sqrt{(x-u)^2 + (y-v)^2 + z^2}$$

This equation can be interpreted as the convolution of the impulse response of free space with the input function E(x,y) [44]. One often considers the Rayleigh-Sommerfeld diffraction integral to be superior over other diffraction theories such as Huygens-Fresnel's, and Kirchhoff's theories. Although both are powerful and adequate to describe the diffraction of the majority of problems these approximations are based on incorrect assumptions about the boundary conditions for the electric and magnetic fields.

The Rayleigh-Sommerfeld integral can be simplified by making further assumptions. In the far distance one can apply the following approximations for the amplitude part of the expression: $ik + \frac{1}{r} \simeq ik$, $\frac{z}{r} \simeq 1$. Furthermore the r in the phase part of the equation can be approximated by: $r \simeq z\left[1 + \frac{1}{2}\left(\frac{x-u}{z}\right)^2 + \frac{1}{2}\left(\frac{y-v}{z}\right)^2\right]$. Substituting these new values in the Rayleigh-Sommerfeld integral gives:

$$E_d(u,v,w) = \frac{1}{2\pi}\iint E(x,y,0) \times \frac{e^{-ikz\left[1+\frac{1}{2}\left(\frac{x-u}{z}\right)^2+\frac{1}{2}\left(\frac{y-v}{z}\right)^2\right]}}{z} \times \frac{z}{z} \times (ik+0)dxdy \qquad (6-2)$$

which can be simplified to:

$$E_d(u,v,w) = \frac{ike^{-ikz}}{2\pi z}\iint E(x,y,0) \times e^{\frac{-ik}{2z}[(x-u)^2+(y-v)^2]}dxdy \qquad (6-3)$$

Substitute z→-z:

$$E_d(u,v,w) = \frac{ke^{ikz}}{2i\pi z}\iint E(x,y,0) \times e^{\frac{i\pi}{\lambda z}[(x-u)^2+(y-v)^2]}dxdy \qquad (6-4)$$

which is presented in [31]. Expanding the exponential term inside the integral, for diffraction between two parallel planes x-y and u-v as shown in image 6-2:

$$E_d(u,v) = \frac{ke^{ikz}e^{\frac{ik}{2z}(u^2+v^2)}}{2i\pi z}\iint E(x,y)e^{\frac{ik}{2z}(x^2+y^2)}e^{-\frac{ik}{2z}(2ux+2vy)}dxdy \qquad (6-5)$$

This equation is called the Fresnel diffraction integral. The inverse of equation (6-5) is called the inverse Fresnel diffraction equation and is given by [47]:

$$E(x,y) = \frac{ike^{-ikz}e^{-\frac{ik}{2z}(x^2+y^2)}}{2\pi z}\iint E_d(u,v)e^{-\frac{ik}{2z}(u^2+v^2)}e^{\frac{ik}{2z}(2ux+2vy)}dudv$$

(6-5b)

Substituting $E_d(u,v)$ in expression (6-5b) with expression (6-5) shows that the integral on the right side of equation 6-5b is indeed E(x,y).

Note that the Fresnel diffraction equation, i.e. equation (6-5) contains a phase factor in front of the integral and a phase factor under the integral. If one considers the projection screen to be placed in infinity, $z >> \frac{k\left(x^2+y^2\right)}{\lambda}$ and $z >> \frac{k\left(u^2+v^2\right)}{2}$, the quadratic phase factors becomes small and it can be ignored. Therefore,

$$E_d(u,v) = \frac{ke^{ikz}}{2i\pi z}\iint E(x,y)e^{-\frac{ik}{2z}(2ux+2vy)}dxdy \qquad (6-6)$$

The integral can be considered to be a scaled Fourier transform of the input function E(x,y).

Figure 6.3: Diffraction between two parallel planes

Positioning a spherical lens with focal length f in front of the x-y plane as shown in the image 6.3 and considering z=f have the same effect. The Fresnel diffraction expression is simplified because of the phase function of the lens $e^{\frac{-ik}{2f}(x^2+y^2)}$ [31]:

$$E_d(u,v) = \frac{ke^{ikf}e^{\frac{ik}{2f}(u^2+v^2)}}{2i\pi f}\iint E(x,y)e^{-\frac{ik}{2f}(2ux+2vy)}dxdy \qquad (6-7)$$

Figure 6.4: Positioning a spherical lens with focal length f in front of the x-y plane to ignore the phase factors

This expression relates the optical field in the focal plane of the lens, $E_d(u,v)$, to the optical field in the input plane, E(x,y), of the setup. The factor in front of the integral consists of a phase factor and constants. If one only considers the intensity of the image,

the phase factor is not relevant. The integral in the equation above is known as a 2-Dimensional Fourier Transform. Therefore one often refers to the setup of Fig. 5-3 as a 1f Fourier transform optical system. Introducing the spatial frequencies $u' = k\frac{u}{f}$, $v' = k\frac{v}{f}$ above equation can be written as:

$$E_d(u', v') = \frac{ke^{ikf}e^{\frac{if}{2k}(u'^2+v'^2)}}{2i\pi f}\Im\big(E(x,y)\big) \qquad (6-8)$$

This is called the Fraunhofer diffraction integral.

The Fourier integral can be separated into two 1-D Fourier integrals. This significantly speeds up the calculations. So, in discrete mode, one can take two 1-D Fast Fourier Transform (FFT) instead of a 2-D Discrete Fourier Transform (DFT):

$$E_d(u, v) = \frac{ke^{ikf}e^{\frac{ik}{2f}(u^2+v^2)}}{2i\pi f}\iint E(x,y)e^{-\frac{ik}{2f}(2ux+2vy)}dxdy \qquad (6-9)$$

$$E_d(u, y) = \frac{ke^{ikf}e^{\frac{ik}{2f}u^2}}{2i\pi f}\int E(x,y)e^{-\frac{ikux}{f}}dx \qquad (6-10)$$

$$E_d(u, v) = e^{\frac{ik}{2f}v^2}\int E(u,y)e^{-\frac{ikvy}{f}}dy \qquad (6-11)$$

The input function E(x,y) of the setup can be realized by shining a parallel laser beam on a mask or a spatial light modulator. Both the amplitude and the phase, or just the amplitude or the phase of the input optical field can be modulated. Various SLM

technologies exist. The Pluto Holoeye liquid crystal modulator employed in this thesis only modulates the phase. The figure below shows a possible setup. The optical field on the SLM is referred to as the kino-form of the far field diffraction pattern. Phase SLMs are currently being investigated to be applied in lens-less overhead projectors. Modulating the phase instead of the amplitude leads to larger energy throughput.

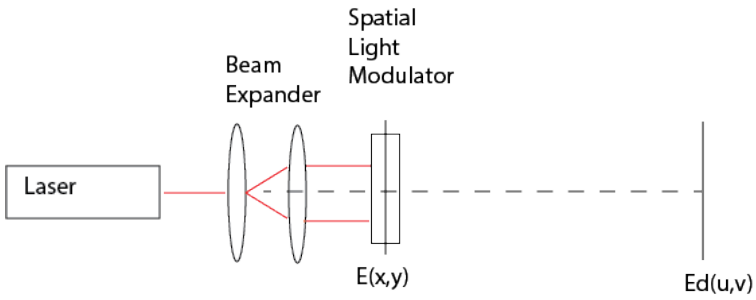

Figure 6.5: Modulating the phase instead of the amplitude using the SLM

It is well known that the phase of a wavefront has a much larger impact on the far field diffraction pattern than its amplitude [44]. The figure below shows an image of the Texas bobcat (Fig. 6.6a) and the old SWT logo (Fig. 6.6b). Assuming a constant phase, the Fourier components (phase and amplitude) of the optical field in the diffracting plane were calculated using the Fraunhofer diffraction theory. The phase functions of both images were swapped and the new far field images were calculated from the Fraunhofer diffraction integral. The far field image calculated from the phase of the SWT logo and the amplitude of the bobcat resulted in an image that resembles the SWT logo (Fig.6.6c). Another combination, i.e. the phase function of the bobcat and the amplitude of the old SWT logo, results in a far field image that looks like the bobcat (Fig. 6.6d).

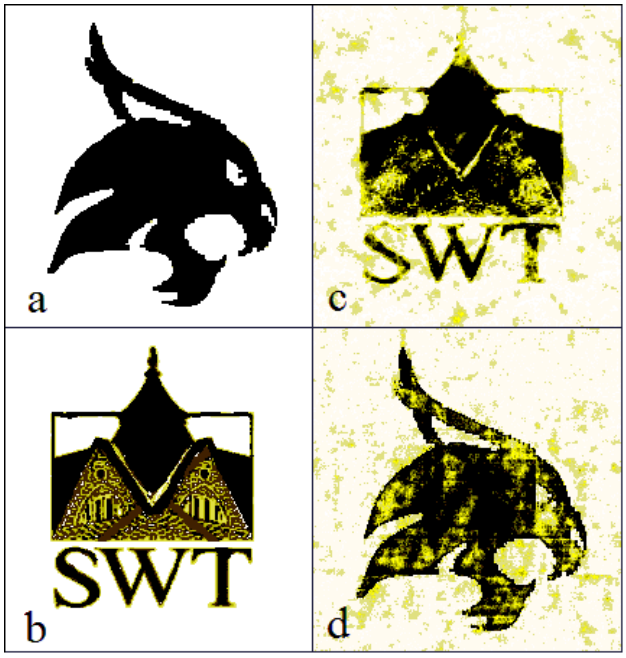

Figure 6.6: (a) The Bobcat logo Texas State University; (b) Old SWT logo; (c) Far field diffraction pattern if one combines the amplitude of the other one

The dominant effect of the phase can be understood if one considers the effect of a lens on plane waves as illustrated in the figure below. A plane wave that is parallel to the optical axis is focused in a point on the optical axis in the focal plane of the lens. Plane waves that enter the lens under an angle, are focused in an off-axis point in the focal plane. In other words bright pixels in the Fraunhofer diffraction pattern indicate the presence of a plane wave diffracted by the SLM in a certain direction. As the Fourier phase component of a delta function (read point spread function) has a constant amplitude through space [45], to generate a single pixel in the Fraunhofer diffraction pattern, the amplitude of the optical field in the diffracting plane should not be varied.

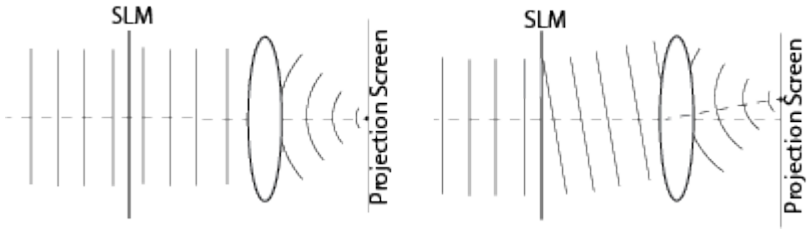

Figure 6.7: The effect of a lens on plane waves

Furthermore if one generates the amplitude and phase spectrum of different images, most amplitude spectra of images are very similar. Most of the energy of the magnitude spectrum is concentrated at the middle and then decays in an exponential manner with increasing frequency. The phase spectrum however is spread out over the completely spectral range and almost equally distributed [46].

Inverse Phase Problem

Using a phase modulator to image a certain pattern on the sample under the objective in the laser beam writer is not straight forward. Optical fields E(x, y) and $E_d(u,v)$ are both complex functions. Furthermore an image is an intensity distribution across a two dimensional surface, so, it only defines the amplitude of $E_d(u,v)$ and not its phase. So, one cannot just take the inverse Fourier transform of $E_d(u,v)$ to find the required phase function E(x,y). First of all, the phase of $E_d(u,v)$ is not known and secondly, there are many E(x,y) functions all with the same far field Fraunhofer diffraction pattern. Assuming that a plane wave of coherent light is incident upon the modulator, one also knows the amplitude of E(x,y). Practically, using a phase modulator, only the phase component of E(x,y) can be made. On the other hand, only the amplitude

component of $E_d(u,v)$ is visible in the u-v plane. Calculating the phase distribution in the x-y plane to have the best quality amplitude or intensity distribution in the u-v plane is a traditional problem. It is has a known solution that was first presented by Gerchberg and Saxton [41]. They calculated the phase function of an electron microscope image from the conventional image and the diffraction pattern by using an iterative approach. The general idea of the Gerchberg-Saxton algorithm is shown in Figure 6.8: the Iterative Fourier loop starts from the SLM side with a uniform constant amplitude distribution and a random phase pattern input (1). The Fast Fourier Transform of the function is calculated (2). The result is a complex function (hologram side) with a certain amplitude component and a certain phase component. The amplitude part is replaced by the desired amplitude pattern that is expected to be seen on the projection screen while the calculated phase is unaltered (3). Then, the Inverse Fast Fourier Transform is taken (4), the result of this calculation is a complex function that contains most of the desired image's information in its phase. Its amplitude is replaced by a uniform constant amplitude distribution (5). This new function when loaded on the SLM produces a better approximation of the desired intensity pattern on the project screen. This calculation process is repeated until the obtained amplitude distribution on the projection screen closely resembles the desired image (6). The calculated phase distribution on the SLM side is the output of the algorithm and when loaded on the SLM phase modulator will create the desired image on the distant projection screen (7).

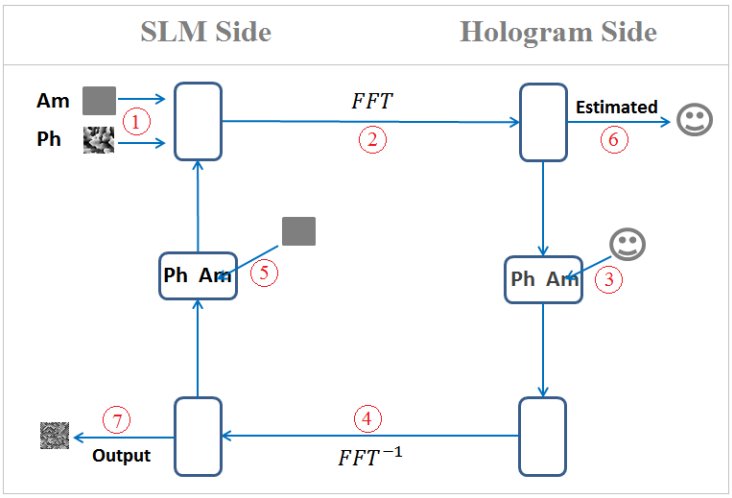

Figure 6.8: Gerchberg-Saxton algorithm diagram

It can be proved that the sum of the squared differences between the pixel's amplitude in the Hologram or SLM planes and the amplitudes of the perfect images decreases after each iterative loop [43]. The algorithm converges and the estimated image as defined in the algorithm, becomes more similar to the desired pattern. Image 6.9 shows the simulation result of Gerchberg-Saxton algorithm performed by Visual Basic. The calculated holograms images are shown after 2, 10, and 20 loops.

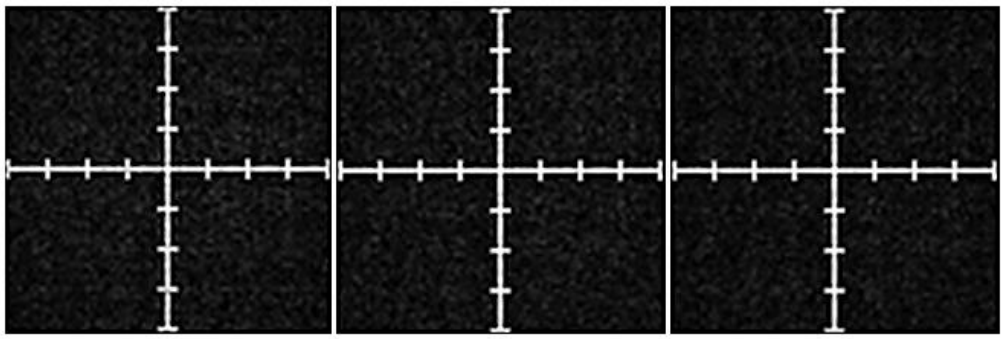

Figure 6.9: The simulation result of Gerchberg-Saxton algorithm

Modified Gerchberg-Saxton Algorithm

For diffraction between two non-parallel planes x-y and u-v as shown in image 6-6, the z in the equation (6-4) is not a constant. Considering the tilting angle of θ degree in the u-v plane,

$$z = z_0 - u\sin(\theta)$$

where z_0 is a constant. After expanding the exponential term inside the integral, the $e^{\frac{ik}{2z}(x^2+y^2)}$ term has variables in both the x-y and the u-v planes. Hence, there is no way to cancel this term by using an optical phase component positioned in the x-y plane.

$$E_d(u,v) = \frac{ke^{ikz}e^{\frac{ik}{2z}(u^2+v^2)}}{2i\pi z}\iint E(x,y)e^{\frac{ik}{2z}(x^2+y^2)}e^{-\frac{ik}{2z}(2ux+2vy)}dxdy \qquad (6-12)$$

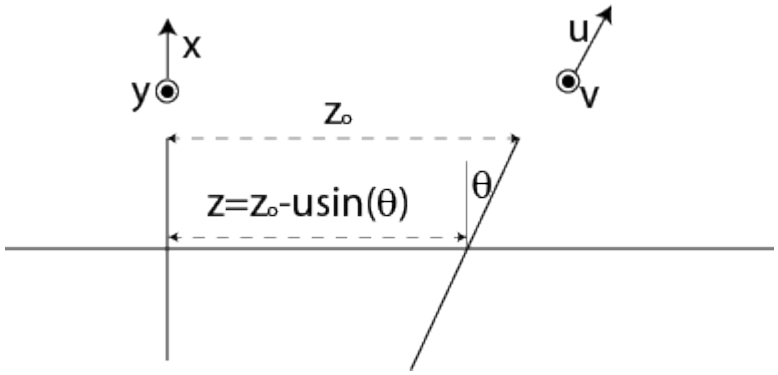

Figure 6.10: The diffraction between two non-parallel planes

Equation (6-4) is changed to the new form using above mentioned z dependance:

$$E_d(u,v) = \frac{e^{ik[z_0 - u.sin\theta]}}{i\lambda[z_0 - u.sin\theta]} e^{\frac{ik}{2[z_0 - u.sin\theta]}[u^2+v^2]} \iint_{-\infty}^{+\infty} E(x,y) e^{\frac{i\pi}{\lambda[z_0 - u.sin\theta]}[(x^2-2ux)+(y^2-2vy)]}\, dx\, dy \qquad (6-13)$$

Note that y is parallel to v, but x and v are not parallel to each other. The integral can be separated in two 1-Dimensional integrals to speed up calculations:

$$G(u,y) = \frac{e^{ik[z_0 - u.sin\theta]}}{i\lambda[z_0 - u.sin\theta]} e^{\frac{ik}{2[z_0 - u.sin\theta]}u^2} \int_{-\infty}^{+\infty} E(x,y) e^{\frac{i\pi}{\lambda[z_0 - u.sin\theta]}[x^2-2ux]} dx \qquad (6-14)$$

$$E_d(u,v) = e^{\frac{ik}{2[z_0 - u.\sin\theta]}v^2} \int_{-\infty}^{+\infty} G(u,y) e^{\frac{i\pi}{\lambda[z_0 - u.sin\theta]}[y^2-2vy]} dy \qquad (6-15)$$

Note that the inverse of equation (6-13) may not exist. If the spatial frequencies on the SLM are very high, the SLM diffracts beams under very large angles, and that light misses the projection plane all together. So, that information is lost. The resolution

of the SLM used in this thesis work is limited, and the maximum deflection angle is +/-11 degrees. So, as long as the angle between the SLM and the projection plane is smaller than 88 degrees, all of the rays diffracted from the SLM are caught by the projection screen and an inverse expression for equation (6-13) should exist.

When considering the inverse diffraction, one should change the optical axis of the system to allow the integral to be separable. The optical axis is now perpendicular to the u-v plane. The orientation of the planes with respect to each other is still θ degrees. Also, the distance between the planes is still z_o (see Fig. 6.11). However, the origin of both the uv-plane and the xy-plane are both shifted to some extent.

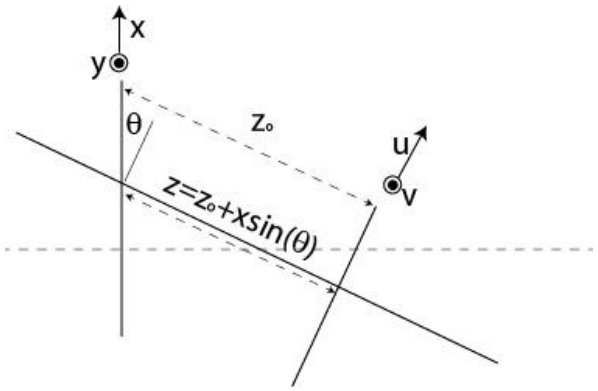

Figure 6.11: The orientation of the planes for inverse diffraction

Using the Fresnel inverse diffraction expression (equation 6.5b), E(x,y) can be expressed in $E_d(u,v)$ as follows:

$$E(x,y) = \frac{e^{ik[z_0 - x.sin\theta]}}{i\lambda[z_0 - x.sin\theta]} e^{\frac{ik}{2[z_0 - x.sin\theta]}[x^2+y^2]} \iint_{-\infty}^{+\infty} E_d(u,v) e^{\frac{i\pi}{\lambda[z_0 - x.sin\theta]}[(u^2-2ux)+(v^2-2vy)]} du\, dv$$

(6-16)

Note that this integral can also be separated in two 1-Dimensional integrals:

$$G_d(x,v) = \frac{e^{-ik[z_0 - x.sin\theta]}}{i\lambda[z_0 - x.sin\theta]} e^{\frac{-ik}{2[z_0 - x.sin\theta]}x^2} \int_{-\infty}^{+\infty} E_d(u,v) e^{\frac{-i\pi}{\lambda[z_0 - x.sin\theta]}[u^2 - 2ux]} du \qquad (6-17)$$

$$E(x,y) = e^{\frac{-ik}{2[z_0 - x.sin\theta]}y^2} \int_{-\infty}^{+\infty} G_d(x,v) e^{\frac{-i\pi}{\lambda[z_0 - x.sin\theta]}[v^2 - 2vy]} dv \qquad (6-18)$$

Note that the xy-coordinate system of equations (6-16), (6-17) and (6-18) is different from the xy-coordinate system of equations (6-13), (6-14), and (6-15). This is also clear from comparing figures 6.9 and 6.10. The origin of the xy-coordinate system of figure 6.10 is shifted up with respect to the origin of figure 6.9's xy-coordinate system's origin.

Discrete Mode Calculations

To calculate the transfer function for any distributions using a processor, all relations should be changed into discrete mode. G (u, y) as defined in equation 6-14 has an integral in general form of:

$$G(u,y) = K_1 \int_{-\infty}^{+\infty} E(x,y) e^{\frac{i\pi}{a+bu}[x^2 - 2ux]} dx \qquad (6-19)$$

where a= λz_0 and b= $-\lambda \sin\theta$ are constants inside the integral, and K_1 contains the terms in front of the integral of equation (6-14). E_d (u, y) as defined on equation 6-15 has an integral in general form of:

$$E_d(u,v) = K_2 \int_{-\infty}^{+\infty} G(u,y) e^{\frac{i\pi}{c}[y^2 - 2vy]} dy \qquad (6-20)$$

where c= λ [z_0-u.sin θ] is a constant inside the integral and K_2 contains the terms in front of the integral of equation (5-15). As the SLM has finite dimensions, E(x,y) is zero outside the optical aperture of the system. So, the infinite boundaries can be replaced by finite boundaries. Also, E(x,y) is not continuous because the SLM is a digital device. So, E(x,y) is pixilated. Assuming that the SLM has $N_{x'}$ pixels in the x-direction and $N_{y'}$ pixels in the y-direction and assuming that the pixels size to be square equal to PS, the pixelated version of E, E', can be written as:

$$E'(x',y') = \sum_{y'=0}^{N_{x'}-1}\sum_{x'=0}^{N_{y'}-1} E(x'PS, y'PS)\, rect(x - x'PS, y - y'PS) \qquad (6-21)$$

which shows that the pixelated version is the convolution of E with the rectangular function, where the rectangular function is defined as:

$$rect(x,y) = \begin{cases} 1 \Rightarrow & 0 < x < PS, \quad 0 < y < PS \\ 0 \Rightarrow & x < 0, \quad PS < x, \quad y < 0, \quad PS < y \end{cases} \qquad (6-22)$$

Assuming that the effect of pixelation is negligible, the rect function can be replaced in above equation by 1. This corresponds to assuming that each pixel is described by a delta function.

E(x,y) is sampled $N_{x'}$ $N_{y'}$ times within the dimensions of the SLM, i.e. $N_{x'}PS \times N_{y'}PS$. Note that based on Nyquist sampling theorem, 1/PS must be twice the highest spatial frequency in E(x,y). In other words the SLM can only be used to make spatial frequencies up to 1/(2*PS). Higher spatial frequencies (read higher diffracted beams) cannot be created by the SLM. Rewriting equation 6.14 and 6.15, gives for the diffraction equations:

$$G'(m,y') = K_1 PS \sum_{x'=0}^{N_{x'}-1} E'(x',y') e^{\frac{i\pi}{a+bm\Delta u}\left[(x'PS)^2 - 2x'PSm\Delta u\right]} \qquad (6-23)$$

$$m = 0, 1, \dots, (N_u - 1)$$

$$E'_d(m,n) = K_2 PS \sum_{y'=0}^{N_{y'}-1} G'(m,y') e^{\frac{i\pi}{c}\left[(y'PS)^2 - 2y'PSn\Delta v\right]}$$

$$m = 0, 1, \dots, (N_u - 1), n = 0, 1, \dots, (N_v - 1) \qquad (6-24)$$

where x' and y' are pixel numbers and m and n are the discrete frequency components belonging to the spatial frequencies mΔu and nΔv. Similarly rewriting 6-17 and 6-18 gives for the inverse diffraction equations:

$$G_d{}'(x',n) = K'_1\,\Delta u \sum_{m=0}^{N_u-1} E_d{}'(m,n)\, e^{\frac{i\pi}{a+bx'PS}\left[(m\Delta u)^2 - 2x'PSm\Delta u\right]} \qquad (6-25)$$

$$x' = 0, 1, \ldots, (N_{x'} - 1)$$

$$E'(x',y') = K'_2 \Delta v \sum_{n=0}^{N_v-1} G_d{}'(x',n)\, e^{\frac{i\pi}{c}\left[(n\Delta v)^2 - 2y'PSn\Delta v\right]} \qquad (6-26)$$

$$y' = 0, 1, \ldots, \left(N_{y'} - 1\right), x' = 0,1, \ldots, (N_{x'} - 1)$$

Note that Δu, Δv, N_u, and N_v need to be chosen so that all diffracted beams are sampled in the uv-plane and none are missed. So the summations in equations (6-25) and (6-26) should be across the complete intervals for which the diffraction pattern on the uv-plane is unequal to zero. Furthermore in order to find a unique solution for E'(x',y') one need to have at least as many samples in the uv-plane as in the x'y' plane, i.e. N_u*N_v should be larger or equal to $N_{x'}$*$N_{y'}$. Only if those two conditions are met, the Nyquist–Shannon sampling theorem can be fulfilled. Note that for an inclined or curved surface the separation of the diffraction orders will be different at different areas of the projection plane. To avoid under sampling, one should use a Δu and Δv small enough to sample the areas of the uv plane with the highest diffraction beam density or one should apply non-uniform sampling techniques. N_u and N_v should be chosen large enough so the whole diffraction pattern is sampled. Note that if further restrictions are imposed on the diffraction pattern, then the Nyquist-Shannon criterion may no longer be a necessary condition for finding a unique E' and full reconstruction of E' is possible with a sub-Nyguist sampling rate [27].

If the relation between the electric field in the SLM plane and the projection plane is described by a Fourier transform function and if it is assumed that N_u=N_v=$N_{x'}$=$N_{y'}$=N and Δu=Δv, it can be shown by using the Convolution Theorem that the relationship between

the pixel size (PS), Δu, and N is given by: N*PS=1/Δu [48]. In this way, the exponential term inside the integral is independent from the sampling rate in the SLM plane (PS) and the sample rate in the projection plane. It simplifies the expressions and speeds up the calculations. However, for the functions (6-19) and (6-20) it can be shown that because of the quadratic term in the exponent, the Convolution Theorem is not justified and a simple expression between PS, Δu, and N may not be found.

The equations (6-23) through (6-26) were implemented in a visual basic program. The validity of the equations were checked in the following three ways:

1. Equations (6-23) and (6-24) were first used to calculate E_d'(m,n) from E'(x',y'). This result and equations (6-25) and (6-26) were used to calculate E'(x',y'). The E'(x',y') found this way was identical to the initial E'(x',y') except for a small shift that could be explained by the shift of the origin of the xy-coordinate system between figures 6.9 and 6.10.
2. Equations (6.23) and (6.24) were used to calculate the diffraction pattern on projection screens placed at different distances from the SLM. The calculated E_d'(n,m) functions were compared with what one would expect using a qualitative physical analysis.
3. Equations (6.23) through (6.26) are based on equations (6.13) and (6.16) which describe the diffraction from a flat plane perpendicular to the optical to a flat inclined plane and its inverse. A special case would be if the tilt angle is equal to zero. In this condition, equation (6-13) for example can be simplified to:

$$G(u,v) = \frac{e^{ikz_0}}{i\lambda z_0} e^{\frac{ik}{2z_0}[u^2+v^2]} \iint_{-\infty}^{+\infty} U(x,y) e^{\frac{i\pi}{\lambda z_0}[(x^2-2ux)+(y^2-2vy)]}\, dx\, dy \qquad (6-27)$$

Equation (6-27) corresponds to the Fersnel diffraction equation which is known from literature.

Implementation and Preliminary Experimental Results

Using the discretized transfer functions and its inverse functions that describe diffraction from a flat plane perpendicular to the optical axis to a flat plane tilted with respect to the

optical axis (equations 6-23, 6-24, 6-25, and 6-26), the modified Gerchberg-Saxton algorithm for diffraction on a tilted projection screen (Fig. 6.12) was implemented in a visual basic program.

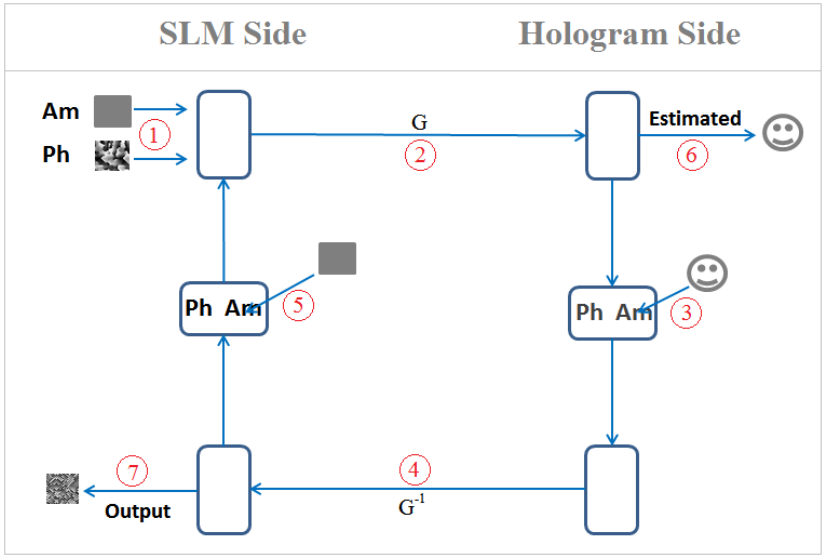

Figure 6.12: The modified Gerchberg-Saxton algorithm diagram

The modified Gerchberg-Saxton visual basic program was used to calculate the phase pattern to create various test patterns on an inclined projection screen. The algorithm appeared to be stable and converging rapidly for all patterns the algorithm was tested with. Some preliminary results are shown in Figure 6.13 for a simple xy-coordinate system on a black background. The images show the estimated diffraction pattern using the optical field that was found after 2 iterations, after 10 iterations, and after 20 iterations.

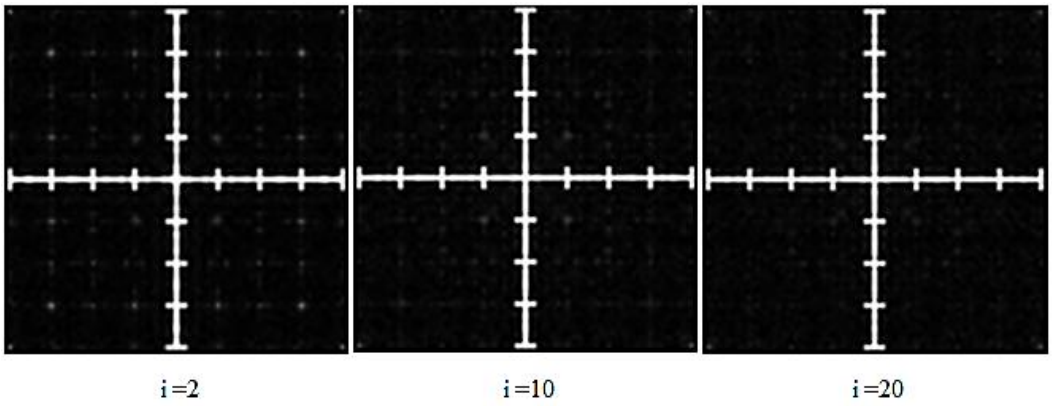

Figure 6.13: Simulation result of Modified Gerchberg Saxton algorithm

The PLUTO SLM setup was used to project the calculated SLM optical field using the modified Gerchberg Saxton algorithm on a screen tilted with the optical axis. The screen was oriented at 41^{o} and located at 60 cm from the SLM. The images shown in Figure 6.14 are taken from the screen using a Canon DSLR camera. Figure 6.14a shows the projected pattern on the screen when the SLM was loaded with the optical field calculated using the normal Gerchberg Saxton algorithm. Figure 6.14c shows that the left of the image is out of focus while Figure 6.14d shows that the right side of the image is in-focus. In the second experiment the SLM was loaded with the optical field that was calculated using the modified Gerchberg Saxton algorithm ($\theta=41^{o}$). Results are shown on Figure 6.14b. Figures 6.14e and 6.13f show that the projected image is in focus on both the left and the right sides of the image and that a small improvement is obtained. The results of Figure 6.14 also show that if the SLM is loaded with the results of the modified Gerchberg Saxtan algorithm, the diffraction pattern on an inclined distant screen resembles the pattern that was used as input of the modified Gerchberg-Saxtan algorithm. So this furthermore provides some verification of equations 6-23 through 6-26.

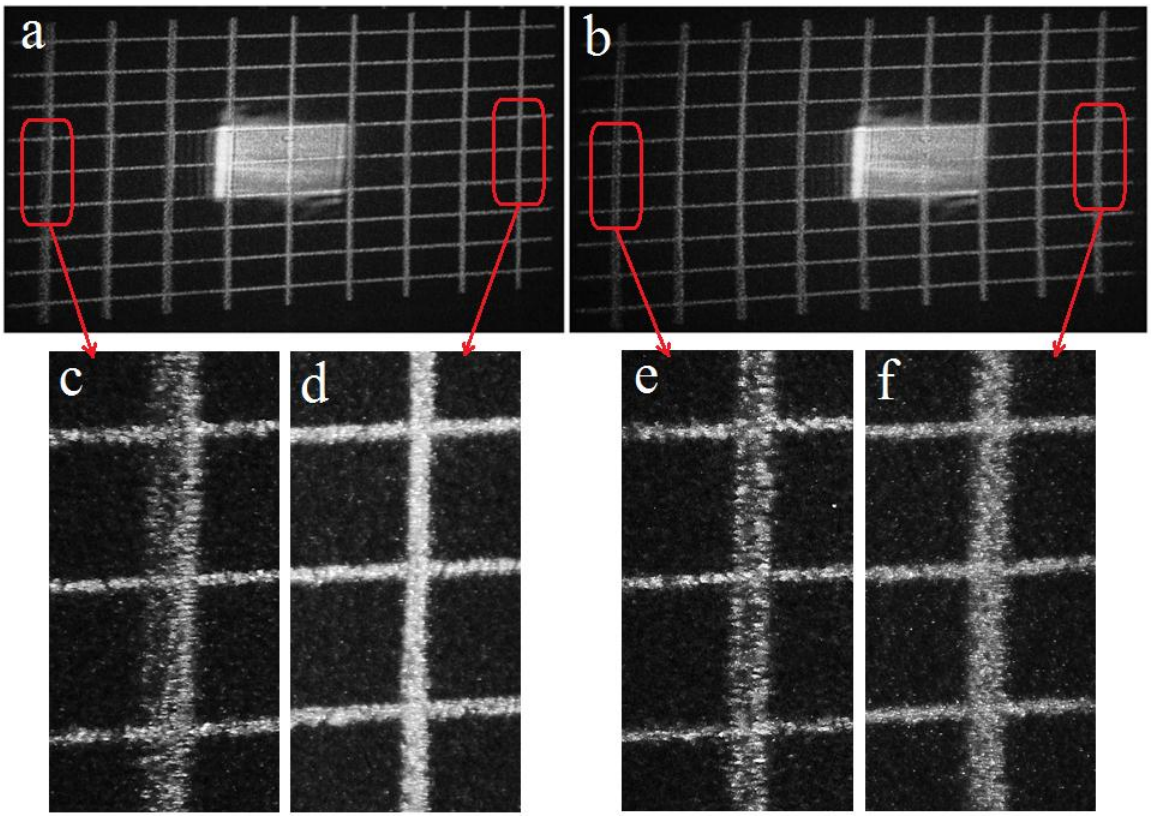

Figure 6.14: Experimental result of Modified Gerchberg Saxton algorithm

CHAPTER VII: CONCLUSION AND RECOMMENDATION FOR FURTHER RESEARCH

Three different techniques were studied in this thesis to shape the laser beam for lithography on curved surfaces using the Holoeye Pluto phase only modulator and the Holoeye LC 2002 twisted nematic modulator.

Limitations on beam shaping, focusing, and imaging using SLM single lenses and SLM multi-lens arrays were defined in terms of optical aberrations, pixel size, SLM size, and SLM modulation depth. In addition to the classical lens aberrations, SLM lenses have three additional contributions to the optical aberration, i.e. effects of quantization, effect of pixelation, and effect of the curvature of the modulator. Although the effect of pixelation can be minimized by choosing an SLM with a small pixel size, theoretically it cannot be nullified as strictly speaking the Shannon-Nyguist sampling condition cannot be fulfilled for a quadratic phase function. Quantization aberration has a significant effect on the center of the lens while the effect of pixelation increases near the lens edges. Small diameter lenses with a large focal distance implemented on the SLM have a small pixelation aberration but they are diffraction limited. Large diameter lenses implemented on the SLM have a negligible diffraction but a large pixelation aberration and their performance is aberration limited. Preliminary experiments that explored the use of an SLM multi lens array whose lenses have different focal distances to improve the depth of focus and image quality for imaging on a curved substrate with detailed surface

topography is disappointing. But, for tilted substrates or for samples that are approximated by several simple step functions, the multi lens approach provides a qualitative improvement. More work is necessary including the introduction of a quantitative measurement method to describe image quality on tilted and curved substrates.

An expression for the phase function of a tilted lens was derived and implemented on the SLM to improve the imaging quality on a tilted surface. This approach requires a real object that is imaged by the SLM lens on the tilted plane. Experimental results show a small improvement. The experiments also showed that the imaging capabilities of an SLM lens are poor when light incident on the SLM is not perpendicular. It is recommended that the tilted lens functions are repeated by designing a compound lens consisting of a tilted SLM lens and one or more standard glass lenses. The design of the compound lens should place the SLM in infinity space, to make sure that light on the SLM is perpendicular to it.

An expression that describes the diffraction from a flat plane perpendicular to the optical axis to a flat plane tilted with respect to the optical axis were derived from the Rayleigh-Sommerfeld diffraction integrals. Also an expression for the inverse function was derived. Both diffraction equations were digitized and could be separated into two 1 dimensional summations significantly reducing the calculation time compared to a straight forward 2D DFT calculation. It was not possible to use FFT for the summations. The derived expressions were used to implement the modified Gerchberg-Saxton algorithm. Preliminary experiments using a simple test pattern show that the SLM optical field calculated with this modified Gerchberg-Saxton does allow for projection on tilted

screens. The algorithm seems to converge and is stable for various test patterns. A similar approach may be used for diffraction from a planar surface to a known curved surface. The modified Gerchberg-Saxton algorithm is more time consuming than the classical Fraunhofer based Gerchberg-Saxton algorithm as one cannot use the FFT algorithm for the former. Although the derivations in chapter 6 show that it is not possible to write the diffraction between two non-parallel planes as a single Fourier transform, it is possible to write it as a Fourier transform (calculation of the diffracted beams), followed by a translation (propagation of the diffracted beams through space), followed by an inverse Fourier transform (reconstruction of the optical field on the inclined diffraction pattern). Using such approach one should be able to use the FFT algorithm to calculate the Fourier and the inverse Fourier transforms, and to significantly reduce the calculation time of the modified Gerchberg-Saxton algorithm. Further investigation of this approach is highly recommended for the future.

APPENDIX A: ACRONYMS AND PHYSICAL QUANTITIES

$\Delta(x,y)$	Thickness Distribution of a Lens
(m,n)	Coordinates in the SLM plane (samples)
(u,v)	Coordinates in the Projection plane (meter)
(x,y)	Coordinates in the SLM plane (meter)
(x',y')	Coordinates in the SLM plane (pixels)
Δn	Birefringence of the Liquid Crystal Molecules
BD	Bit Depth of the SLM
C	Allowable Circle of Confusion
DFT	Discrete Fourier Transform
DOF	Depth of Focus
d_w	Width of Image
E	Continuous Electric Field in the SLM Plane
E'	Sampled Electric Field in the SLM Plane
Ed	Continuous Electric Field in the Projection Plane
Ed'	Sampled Electric Field in the Projection Plane
f	Focal Length of the Lens
F/#	f Number
FFT	Fast Fourier Transform
GRIN Lens	Gradient Index Lens
GV	Grayscale Pixel Value
LCD	Liquid Crystal Display
MD	Modulation Depth of the SLM
N.A. or NA	Numerical Aperture

Nu	Number of Samples in Diffraction Plane (in u direction)
Nv	Number of Samples in Diffraction Plane (in v direction)
Nx'	Size of SLM in x direction (pixels)
Ny'	Size of SLM in y direction (pixels)
PS	Pixel Size
R_1	radii of surface curvature of the first refracting surface
R_2	radii of surface curvature of the 2nd refracting surface
S_0	Object Distance
SLM	Spatial Light Modulator
VGA	Video Graphics Array Interface(15pin D-subminiature connector)
α	a constant that defines the focal length (proportional to 1/f)
β	grayscale value at the center of a lens function
Δ_o	Lens Thickness at the center
Δu	Sample distance in Projection Plane (in u direction)
Δv	Sample distance in Projection Plane (in v direction)
Θ	Tilting Angle
λ	wavelength
$\varphi(x,y)$	phase shift on a ray passing through lens position (x,y)

REFERENCES

[1] Zongsong Gan, Yaoyu Cao, Richard A. Evans, Min Gu, “Three-dimensional deep sub-diffraction optical beam lithography with 9 nm feature size, Nature Communications (2013).

[2] Hansotte, Eric J., Carignan, Edward C., Meisburger, W. Dan, High speed maskless lithography of printed circuit boards using digital micromirrors, Proc. SPIE 7932, 2011, doi:10.1117/12.875599.

[3] D. Gil, D.J.D. Carter, R. Menon, X. Tang, H. I. Smith, "Parallel maskless optical lithography for prototyping, low-volume production, and research", J. Vac. Sci. Technol. B 20(6), 2597-2601 (2002).

[4] N. Takeda, “Ball Semiconductor Technology and Its Application to MEMS”, Proceedings of MEMS 2000, pp.23-27, Miyazaki, Japan (Jan. 2000); Takeda N, MEMS applications of ball semiconductor technology, Stanford University, US–Asia Technology Management Center, Spring 2001 Seminar Series.

[5] Kohei Hashimoto, Yoshihisa Kaneko, Toshiyuki Horiuchi, “Projection lithography onto overall cylindrical surfaces”, Microelectronic Engineering 83 (2006) 1312-1315.

[6] Yigui Li, Susumu Sugiyama, “Fabrication of microgratings on PMMA plate and curved surface by using copper mesh and X-ray lithography mask”, Micrsyst. Technol. (2007) 13, 227-230.

[7] O.V. Gritskevich, N.A. Meshcheryakov, Yu V. Pod'yapol'skii, "Precission laser processing of curve surfaces of revolution", Quantum Electronics 26(7), 644-646.

[8] William R. Childs, Ralph Nuzzo, "Patterning of Thin-Film Microstructures on Non-Planar, Substrate Surfaces Using Decal Transfer Technology", Adv. Mater. 2004, 16, no 14, 1323-1327.

[9] Yung-Pin Chen, Yuet-Ping Lee, Jer-Haur Chang, Lon A. Wang, "Fabrication of concave gratings by curved surface UV-nanoimprint lithography", J. Vac. Sc. Technol. B 26 (5) 1008, 1690-1695.

[10] O. Lima, L. Tan, A. Goel, M. Negahban, "Creating micro- and nanostructures on tubular and spherical surfaces", J. Vac. Sci. Technol. B 25 (6), 2007, 2412-2418.

[11] Rebecca J. Jackman, Scott T. Brittain, Gerge M. Whitesides, "Fabrication of Three-Dimensional Microstructures by Electrochemically Welding Structure Formed by Microcontact Printing on Planar and Curved Substrates", J. Microelectromechanical Systems 7, 2, 1998, 261-266.

[12] Zhaohui Yang, James Leger, "Fabrication of large-sag aspheric miro-optics with nanometer accuracy using electron-beam lithography on curved substrates", Optical Engineering 45 (4), 043401 (April 2006).

[13] Hongxin Zhang, Zhenwu Lu, Fenguou Li, "Fabrication of a curve linear grating by using a laser direct writer system", Optics Communications 266 (2006) 249-252.

[14] Sean Snow, Stephen Jacobsen, "Microfabrication processes on cylindrical substrates – Part II: Lithography and connections", Microelectronic Engineering 84 (2007) 11-20.

[15] Daniela Radtke, Jacques Duparre, Uwe D. Zeitner, Andreas Tunnermann, "Laser lithographic fabrication and characterization of a spherical artificial compound eye", Optics Express 15, n, 2007, 3067-3077.

[16] Long-jiang Chen, Yi-yong Liang, Kai-wei Wang, Jian-bo Luo, Chun-hui Zhang, Jing-yu Liang, Guo-guang Yang, Research on the optical field distribution and micro-fabrication model in convex-surface laser lithography, Optics Communications, Volume 283, Issue 12, 15 June 2010, Pages 2631-2639, ISSN 0030-4018, 10.1016/j.optcom.2010.02.030.

[17] Lenny A Romero, María S Millán and Elisabet Pérez-Cabré, Optical implementation of multifocal programmable lens with single and multiple axes, 2011 J. Phys.: Conf. Ser. 274 012050 doi:10.1088/1742-6596/274/1/012050

[18] "Sample topography measurements by a novel image processing algorithm", Bryant Aaron , Dan Tamir , Javad R. Gatabi , Wilhelmus Geerts , R.K. Pandey, Joint Spring 2012 Meeting of the Texas Sections of the APS and AAPT and Zone 13 of the SPS, Volume 57, Number 2, San Angelo, Texas, 2012.

[19] "Three Dimensional Surface Topography Using LCD Pattern Transfer Method", Javad R. Gatabi ,Wilhelmus Geerts , Bryant Aaron , Dan Tamir , R.K. Pandey, Joint Spring 2012 Meeting of the Texas Sections of the APS and AAPT and Zone 13 of the SPS, Volume 57, Number 2, San Angelo, Texas, 2012.

[20] Geoffrey F. Miller, B.S., a Fast Fourier Transform Approach to Finding the Thickness of Single-Layer Thin Films with Slowly Varying Indices of refraction and Negligible Absorption Coefficients, Theses for Master of SCIENCE, 2012.

[21] Mohammadreza Riahi, Hamid Latifi, Optica Applicata, Vol. XLI, No. 3, 2011, "Fabrication of a 2D thermally tunable reflective grating for measuring a CO2 laser beam profile".

[22] K. Iwasaki, H. Mochizuki, H. Umezawa, M. Inoue, IEEE TRANSACTIONS ON MAGNETICS, VOL. 44, (2008), pp. 3296-3299, "Practical Magneto-Optic Spatial Light Modulator With Single Magnetic Domain Pixels".

[23] Johan A. Neff, Ravindra A. Athale, Sing H. Lee, "Two dimensional Spatial Light Modulators: A Tutorial", Proc. Of the IEEE 78 (1990), pp. 826-855.

[24] Lazarev, G., Hermerschmidt, A., Krüger, S., Osten, S. (2012). LCOS Spatial Light Modulators: Trends and Applications in Optical Imaging and Metrology: Advaced Technologies. Wiley VCH Verlag GmbH&Co. KGaA.

[25] Mukohzaka N, Yoshida N, Toyoda H, Kobayashi Y, Hara T; Diffraction efficiency analysis of a parallel-aligned nematic-liquid-crystal spatial light modulator, Appl Opt. 1994 May 10;33(14):2804-11. doi: 10.1364/AO.33.002804.

[26] Li FH, Mukohzaka N, Yoshida N, Igasaki Y, Toyoda H, Inoue T, Kobayashi Y, Hara T; Phase modulation characteristics analysis of optically-addressed parallel-aligned nematic liquid crystal phase-only spatial light modulator combined with a liquid crystal display, OPTICAL REVIEW; MAY-JUN, 1998, 5 3, p174-p178, 5p.

[27] Yasuhiro Takaki, Hotroshi Ohzu; Liquid-crystal active lens: a reconfigurable lens employing a phase modulator, Optics Communic. 126 (1996) 123-124.

[28] Norihiro Fukuchi, Ye Biqing, Yasunori Igasaki, Narihiro Yoshida, Yuji Kobayashi, Tsutomu Hara; Oblique-Incidence Characteristics of a Parallel-Aligned Nematic-Liquid-Crystal Spatial Light Modulator, Optical Review, 2005, Volume 12, Issue 5, pp 372-377.

[29] Francesco Difato, Marco Dal Maschio, Riccardo Beltramo, Axel Blau, Fabio Benfenati, Tommaso Fellin; Spatial Light Modulators for Complex Spatiotemporal Illumination of Neuronal Networks, Neuromethods,Volume 67, 2012, pp 61-81.

[30] Akondi Vyas, M B Roopashree, B Raghavendra Prasad, Digital long focal length lenslet array using spatial light modulator, proceedings of the International Conference on Optics and Photonics, Chandigarh, India, (2009), arXiv:0911.0821.

[31] Joseph Goodman, Introduction to Fourier Optics, 2004, ISBN-10: 0974707724, ISBN-13: 978-0974707723.

[32] Xiang Shoua, Lugang Baib, Xiuyan Guoa, Single-lens equivalent systems for Grin lenses, Optik, Volume 122, Issue 9, May 2011, Doi:10.1016/j.ijleo.2010.04.025.

[33] Xiaohong Sun, Hui Ma, Hai Ming, Zhiqiang Zheng, Jiwen Yang, Jianping Xie, The measurement of refractive index profile and aberration of radial gradient index lens by using imaging method, Optics & Laser Technology 36 (2004) 163 – 166, doi:10.1016/j.optlastec.2003.07.003.

[34] Eddy C. Tam, Shaomin Zhou, Mike R. Feldman, Spatial-light-modulator-based electro-optical imaging System, Applied Optics 31 (1992) 578-580.

[35] Frank L. Pedrotti, Leno S. Pedrotti, Leno M. Pedrotti, Introduction to Optics. , ISBN 0-13-149933-5, 2007.

[36] Microcope units and Objectives: (UV, NUV, VISIBLE & NIR region), Catolog NO E4191-378, Mitutoyo)

[37] Harold M. Merklinger, The Scheimpflug Principle—Part I- Part IV, Shutterbug, November 1992.

[38] J. C. Tung, H. C. Liang, C. H. Tsou, K. W. Su, Y. F. Chen, Flexible generation of optical beams with quasicrystalline structures via astigmatism induced by a tilted lens, Applied Physics B, December 2012, Volume 109, Issue 4, pp 593-597.

[39] Max Born, Emil Wolf, Principles of Optics: Electromagnetic Theory of Propagation, Interference and Diffraction of Light, 7th edition, Cambridge University Press, 2010, ISBN-13 978-0-521-64222-4.

[40] Nuri Delen; A new FFT based method for general scalar diffraction calculations, ISBN 9780599742246, 0599742240, University of Colorado at Boulder, PHD Dissertations, 2000.

[41] T Haist, M Schönleber, H.J Tiziani, Computer-generated holograms from 3D-objects written on twisted-nematic liquid crystal displays, Optics Communications, V 140, Issues 4–6, 1997, P 299-308.

[42] R. W. Gerchberg, W. O. Saxton, A Practical Algorithm for the Determination of Phase from Image and Diffraction Plane Pictures, OPTIK, Vol. 35 (No.2) 237-246 (1972).

[43] James E. Harvey, Fourier treatment of nearfield scalar diffraction theory, Am. J. Phys. 47 (11) 1979, 974-980.

[44] A. V. Openheim, J. S. Lim, “The importance of phase in signals”, Proceedings of the IEEE 69, 5, pp. 529-541, 1981; Nikolay Skarbnik, Yehoshua Y. Zeevi, Chen Sagiv, “The importance of Phase in image processing”, CCIT report #773, 2010, Irwin and Joan Jacobs Center for communication and information technologies.

[45] Roger L. Eason, Jr., Fourier Methods in Imaging, Wiley, 2010, ISBN 9780470689837.

[46] A. Torrlba, Al. Oliva, “Statisics of natural image categories”, Network, Vol 14, 3, pp. 391-413 (2003).

[47] Okan K. Ersoy, Diffraction Fourier Optics and Imaging, Wiley Interscience, 2007, ISBN 978-0-471-23816.

[48] Mark H. Richardson, Fundamentals of the discrete Fourier Transform, Sound & Vibration Magazine, 1978.

[49] M.A. Davenport, M.F. Duarte, Y.C. Eldar, G. Kutyniok, "Introduction to Compressed Sensing," in “Compressed Sensing: Theory and Applications”, Yonina C. Eldar, Gitta Kutyniok Cambridge University Press, 2012.

VITA

Javad Rezanezhad Gatabi was born in Mashhad, Iran, on September 5, 1986, the son of R. Rezanezhad Gatabi and Z. Esmaeilpour Ghomi. After completing his work at National Organization for Development of Exceptional Talents (NODET) High School, Babol, Iran, in 2003 and NODET University Preparatory School, Babol, Iran, in 2004, he entered the Iran University of Science and Technology (IUST), Tehran, Iran, in Fall 2004. He received his Bachelor of Science in Electrical Engineering-Electronics from IUST in 2010. In January 2011, he entered the Graduate College of Texas State University.

Permanent email address: jrgatabi@yahoo.com

This thesis was typed by Javad Rezanezhad Gatabi.